IOP PUBLISHING JOURNAL OF PHYSICS D: APPLIED PHYSICS

J. Phys. D: Appl. Phys. **46** (2013) 025401 (20pp) doi:10.1088/0022-3727/46/2/025401

Reactive fluxes delivered by dielectric barrier discharge filaments to slightly wounded skin

Natalia Yu Babaeva and Mark J Kushner[1]

University of Michigan, Department of Electrical Engineering and Computer Science 1301 Beal Ave., Ann Arbor, MI 48109, USA

E-mail: nbabaeva@umich.edu and mjkush@umich.edu

Received 30 August 2012, in final form 2 November 2012
Published 5 December 2012
Online at stacks.iop.org/JPhysD/46/025401

Abstract

The application of atmospheric-pressure plasmas to human tissue has been shown to have therapeutic effects for wound healing and in treatment of skin diseases. In this paper, we report on a computational study of the intersection of plasma filaments in a dielectric barrier discharge (DBD) with a small wound in human skin in the context of plasma medicine. The wound is represented as a small cut in the epidermal layer of cells. Intracellular structures and their electrical properties were incorporated into the two-dimensional computational mesh in order to self-consistently couple gas phase plasma transport with the charging of the surface of the wound. We quantify the fluxes of reactive oxygen and nitrogen species, ions and photons produced in or diffusing into the wound as might occur during the first few discharge pulses of treatment. Comparison is made to fluxes predicted by global modelling. We show that the relative location of the plasma filament with respect to the wound is important on plasma time scales (ns) for ions and photons, and for radicals directly produced by electron impact processes. On the longer-term diffusion time scales (ms) the position of the plasma filament relative to the wound is not so critical. For typical DBD conditions, the magnitude of these fluxes to the cellular surfaces corresponds to fluences of radicals nearly equal to the surface site density. These results imply that the biological reactivity is limited by reaction probabilities and not the availability of radical fluxes.

(Some figures may appear in colour only in the online journal)

1. Introduction

Non-equilibrium, atmospheric-pressure plasma treatment of living tissue is being used in a variety of processes collectively called plasma medicine [1–4]. These processes may involve direct contact of a non-equilibrium plasma with living cells for sterilization or therapy. Applications include disinfection [5–7], regulation of cell attachment [8–10], blood coagulation [11], induction of apoptosis in malignant tissues and cancer therapy [12–14] and wound healing [1–3]. These applications are partly based on the high bactericidal effectiveness of plasmas and partly due to the plasma's ability to conformally cover small features [15–17].

The therapeutic effects of the plasma, for example, on wound healing, are attributed to the production of radicals which intersect with biological reaction chains, activation energy of ions and photons, and the intracellular production of electric fields [1–4, 18–21]. The results of animal studies and clinical trials have shown that NO generated by a plasma is effective in tissue disinfection and regulating inflammatory processes associated with acute and chronic wounds [20]. The fluxes of radicals are generally classified as reactive oxygen species (ROS)—including O, $O_2(^1\Delta)$, OH, H_2O_2, O_3, and reactive nitrogen species (RNS), including NO, NO_2, HNO_x. Optimizing these biomedical processes depends on the ability to produce the desired fluxes of radicals and charged species and control their transport to the wound [22, 23].

Two approaches are being followed in the use of non-thermal atmospheric-pressure plasmas in medicine. In the first, the plasma is produced remotely, and its afterglow is delivered in a plume to the tissue [17, 24]. In the second, plasmas

[1] Author to whom any correspondence should be addressed.

are generated in direct contact with living tissue, usually in the form of dielectric barrier discharges (DBDs) where the applicator contains the powered electrode and the tissue is the counter electrode [11, 12]. DBDs are often filamentary where the primarily radicals are produced in the head of the filaments during the short time of propagation of the plasma filament across the few mm gap between the applicator and the tissue, that is 1–2 ns. When the filament strikes the tissue, very much like a conventional DBD, the plasma may spread laterally as the tissue charges. This extends both the duration of the filament and the spatial domain over which primary radicals are produced.

Typical DBDs operate at many hundreds of Hz to tens of kHz, resulting in intra-pulse afterglow periods of hundreds of microseconds to a few ms. The delivery of radicals, ions and photons to the tissue occurs over three time scales. The first is the duration of the filament, during which primary electron impact and ion–molecule reactions occur—a few to 10 ns. During this time, the ion and photon fluxes are maximum and radical fluxes to the tissue result from electron impact processes in close vicinity to the surface. The second time scale is a diffusion scale of the intra-pulse afterglow, up to many ms. During this time, ion and photon fluxes are small but neutral radical fluxes may increase (or decrease) based on transport and chemical reactions. The third time scale could be up to tens of seconds. The fluxes of plasma produced species may, in fact, evolve over many seconds of plasma application to the tissue due to slow accumulation of mildly reactive reaction products.

Deploying plasmas for medicine will likely require some aspect of control to insure reproducibility. In this regard, having a predictive knowledge of the fluxes of radicals and ions to the tissue for device operating conditions would be helpful—and so modelling of atmospheric-pressure plasma chemistry has been pursued with the goal of obtaining this predictive capability. Zero-dimensional global models of He/O_2 and Ar/O_2 atmospheric-pressure glow discharges solving time-dependent particle and power balance equations have been developed by Park *et al* [25]. They found that atomic oxygen radicals and $O_2(^1\Delta)$ fluxes were typically maximized with only a few per cent O_2 in the flow. Liu *et al* [26] developed a model of a low-temperature atmospheric-pressure diffuse He/O_2 glow discharge. Their detailed models include 21 species and 267 reactions. Based on analysis of their results, a subset of species and reactions was selected to create simplified models that are able to capture the main physicochemical processes in the discharge, but with reduced numerical complexity.

For air based plasmas, the humidity of the air can have a significant effect on the ROS incident onto the tissue. To quantify these processes, Liu *et al* [27] developed global models of a low-temperature atmospheric-pressure diffuse He/H_2O glow discharges. The main species and reactions were identified, and simplified models capable of capturing the main physicochemical processes in $He + H_2O$ discharges were suggested. Water clusters of growing size were found to be the dominant charged species when the water concentration is above $\approx$100 ppm.

Modelling of atmospheric-pressure air plasmas in the context of plasma remediation of toxic gases [28–30], plasma aided combustion [31–33] and aeronautical flow control [34] has significantly improved our understanding of this complex plasma chemistry. The current understanding of dry-air plasmas was discussed in modelling by Kossyi *et al* [35]. The ion chemistry of humid air plasmas was summarized by Sieck *et al* [36] and for neutral chemistry by Herron and Green [37].

Recent modelling of DBD excitation of air plasmas in the context of plasma medicine using a multi-zone global model has been performed by Sakiyama *et al* [38] and Shimizu *et al* [39]. They have shown that, in the absence of forced gas flow, the ROS and RNS species can evolve over hundreds of seconds, a result of slow reactions between mildly reactive species in the gas phase, which nevertheless may be biologically important. To address the dynamics of He/O_2 jets propagating into humid air, Murakami *et al* developed a global model of this system [40, 41]. They found that the ion chemistry of the jet was dominated by water-cluster ions (both positive and negative) with air diffusion into the jet of only 500 ppm.

In this paper, we discuss results from a computational investigation of the production and delivery of photons, ions, ROS and RNS to a small dry wound in the epidermis of human skin by a DBD on plasma and intra-pulse time scales, and time scales approaching seconds. We show that the relative location of the plasma filament with respect to the wound determines the symmetry of treatment on a short plasma time scale, particularly for ions and photons. The position of the filament relative to the filament is not so critical on the long-term diffusion scale and even less so on the longer time scale. The plasma spreads on the surface of the skin and into the wound, the latter being limited by the requirement that the plasma Debye length be smaller than the dimensions of the wound.

The model and reaction mechanism are discussed in section 2. Radical, ion and photon fluxes delivered to the wound when the filament is directly over the wound are discussed in section 3, and fluxes for when the filaments are to the side of the wound are discussed in section 4. A comparison to global modelling appears in section 5. Our concluding remarks are in section 6.

2. Description of the model

The model used in the study is essentially the same as that described in [42]. The model, *nonPDPSIM*, is a multi-fluid 2D hydrodynamics simulation in which transport equations for all charged and neutral species and Poisson's equation are integrated as a function of time. Poisson's equation, transport equations for conservation of the charged species, and the surface charge balance equation, are simultaneously integrated using a Newton iteration technique. Updates of the charged particle densities and electric potential are followed by an implicit update of the electron temperature by solving the electron energy equation for average energy ε. The electron transport coefficients and rate coefficients for bulk electrons as a function of ε, are obtained by solving the zero-dimensional Boltzmann's equation for the electron energy distribution to capture the non-Maxwellian nature of the electron swarm. These values are stored in tabular form and interpolated during

execution of the code. The tables are periodically updated to reflect changes in species densities. The update of electron temperature is then followed, in a time splicing manner, with an implicit update of neutral particle densities. In this work, we have considered only diffusional transport of neutral species, and secondary electrons from surfaces are directly included as sources in the fluid equations.

Photoionization by streamer generated radiation producing electrons ahead of the avalanche front is important to the propagation of positive streamers [42–47]. Our approach to photoionization is based on line-of-sight propagation of UV ionizing radiation generated by high lying excited states that are produced largely in the high E/N in the avalanche front. The UV radiation is absorbed (without producing ionization) over a specified mean-free-path which determines its extent beyond its origin. Photoionization occurs by absorption of UV radiation by selected species. Radiation transport is addressed using a propagator, Green's function method which also provides photon fluxes to surfaces. We assumed that photoionization occurs by absorption by O_2 of photons emitted by $N_2(b\,^1\Pi)$ and $N_2(b'\,^1\Sigma)$ in the wavelength range 98–102 nm. The non-ionizing absorption cross section was approximated as 2×10^{-17} cm^2 while that for the ionizing cross section is 10^{-18} cm^2. (See, for example, [43] and references therein.)

The gas phase reaction mechanism used in the paper is based on that described in [48] with a reduction in the number of species to be compatible with the increased computational load of a 2D simulation. The primary simplifications were in the reduction in the variety of ions (for example, eliminating the water-cluster ions, NO_x^-, O_3^-) and in the elimination of neutral species which require longer periods of time to generate. These latter species include N_2O_4, N_2O_5, HNO_2, HNO_3. The gas mixture is atmospheric-pressure humid air $N_2/O_2/H_2O = 79/20/1$ at 300 K. The species included in the reduced reaction mechanism are: N_2, N_2^*, N_2^{**}, N_2^+, N, N_4^+, O_2, O_2^*, O_2^+, $O_2(^1\Sigma)$, O_2^-, O^-, O, O^+, O_3, NO, NO^+, NO_2, H_2O, H_2O^+, H_2, H, OH, HO_2, H_2O_2 and electrons. The number of reactions between these species is 135. The states N_2^* and N_2^{**} are nominally $N_2(A\,^3\Sigma)$ and $N_2(b\,^1\Pi, b'\,^1\Sigma)$ though the latter is treated as a lumped state including transitions higher than $N_2(A\,^3\Sigma)$. The state O_2^* is nominally $O_2(^1\Delta)$ but is also intended to be a lumped state including excitation to higher levels. We assumed that all ions neutralized on surfaces and returned to the gas phase as their neutral counterpart. Electrons and ions deposit their charge on bounding surfaces with unity probability. We otherwise assumed that all surfaces were mildly reactive with boundary and sticking coefficients listed in table 1.

A schematic of the geometry used in this study is shown in figure 1. The entire computational domain is 0.6×0.55 cm^2 and includes the majority of the thumb, as shown in figure 1(*a*). The thumb does not touch the boundaries of the computational domain and is at a floating potential as in experiments. The bottom, left and right boundaries of the computational domain are grounded and the top boundary coincides with the powered electrode. Plasma is applied to a thumb, which serves as a floating electrode, with the small wound. The upper powered electrode, positioned over the wound, is covered with a 0.8 mm thick dielectric ($\varepsilon_r = 4$). The plasma processes that produce the radical fluxes occur within the diameter of the filament (a few hundred of μm), which is more than a factor of ten smaller than the lateral dimensions of the mesh. As such, we have confirmed that the boundaries of the mesh are sufficiently far away that the predicted plasma properties are not significantly affected.

Table 1. Surface reaction probabilities [27].

Surface reaction	Reaction probability
N_2^*+ Surface → N_2	0.5
N_2^{**}+ Surface → N_2	0.5
N + Surface → 0.5 N_2	0.01
$O_2(^1\Delta)$ + Surface → O_2	4.0×10^{-4}
$O_2(^1\Sigma)$ + Surface → O_2	0.02
O + Surface → 0.5 O_2	0.02
O_3 + Surface → O_3	1.0
H_2 + Surface → H_2	1.0
H + Surface → H	1.0
OH + Surface → OH	1.0
NO + Surface→ NO	1.0
NO_2 + Surface→ NO_2	1.0
H_2O_2 + Surface→ H_2O_2	1.0
HO_2 + Surface→ HO_2	1.0

Non-plasma materials are assigned appropriate permittivities and conductivities, and Poisson's equation is solved throughout the plasma and non-metal materials. Continuity equations for charge density are also solved on the surface of and inside non-metal surfaces. The end result is that non-metal surfaces naturally will acquire, in a steady state, the floating plasma potential. (Although not used here, the same technique can be used to represent electrically floating metals by treating those materials as highly conductive dielectrics.)

The unstructured mesh uses triangular elements. The mesh consists of more than 11 000 nodes of which more than 4000 are in the plasma. Most of the remaining nodes are used to define the geometry of the cells. The region where the filaments propagate and strike the wound is refined to have elements with smaller dimensions that the more remote regions of the mesh. The smallest distances between the nodes in the gas phase in the centre of the streamer are about 9 μm, decreasing to less than 1 μm inside the wound. In the periphery of the mesh where plasma does not occur the mesh size is as large as 80 μm.

The skin structure consists of a thin outer layer, the epidermis and an inner layer, the dermis. Four layers of cells in the epidermis are resolved. The wound is a small slice in the skin to the dermis which exposes live cells to the plasma. This wound is dry and shallow, and may represent later stages of wound healing. Only a small patch of the epidermis is resolved on a cellular basis. The smallest wound dimension is of the order of 8 μm, which corresponds to a single missing cell at the bottom of the wound. The cellular structures are represented as lossy dielectrics with conductivities and permittivities appropriate for biological tissue. Cell membranes have low conductivity ($8.7 \times 10^{-8}\,\Omega^{-1}\,$cm^{-1}) while cytoplasm and nucleoplasm have high conductivity (5×10^{-3} and $3 \times 10^{-5}\,\Omega^{-1}\,$cm^{-1}, respectively) [49, 52, 53]. The values of permittivity and conductivity used in the model are listed in table 2. The origin

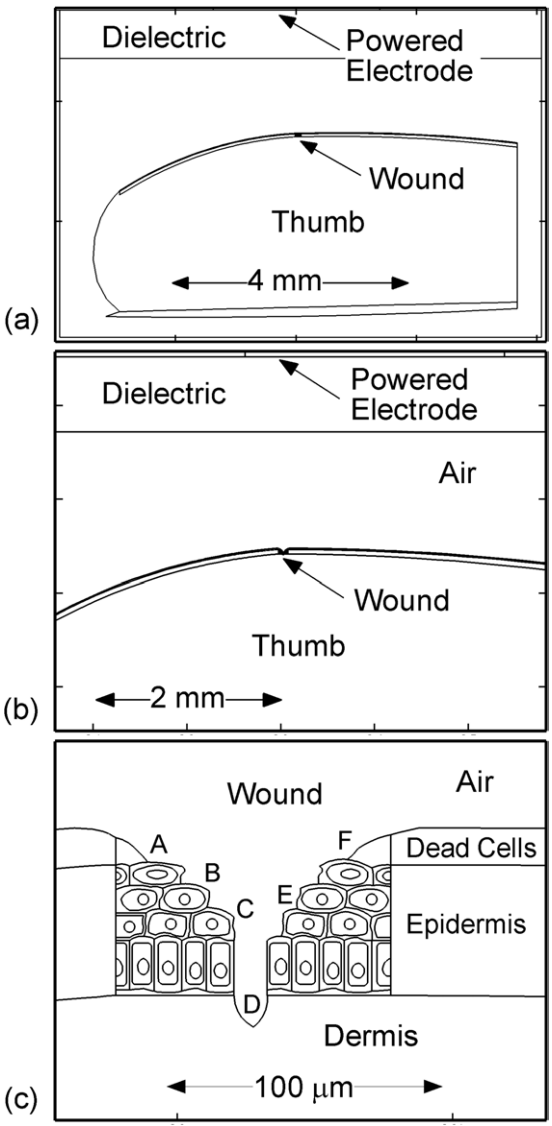

Figure 1. Schematic of the model geometry for DBD treatment of wounded human skin. (*a*) Entire computational domain. (*b*) Vicinity of the wound showing local curvature and the electrode. The entire computational domain is 6 mm × 5.5 mm. The thumb serves as a floating electrode while the upper electrode is powered. The wound is represented as a small cut in the epidermis layer. (*c*) Enlargement of the wound showing the top layer of dead cells, epidermis and dermis. The smallest wound dimension is of the order of 8 μm (bottom of the wound). Fluxes and fluences will be plotted in subsequent figures along the surface of the wound. The letters A to F are benchmarks along the surface to guide the reader in correlating fluxes to features in the wound.

of these values are discussed in detail in [49]. Fluxes and fluences will be plotted in subsequent figures along the surface of the wound. The letters A to F in figure 1(*c*) and subsequent figures are benchmarks along the surface to guide the reader in correlating fluxes to features in the wound.

The negative filaments are launched by artificially having a small amount of electron emission from the upper dielectric from a single mesh point (1 A cm^{-2}, or total current of about 6×10^{-4} A). The filament is then naturally sustained by secondary emission from the dielectric produced by photons and ions. The secondary electron emission coefficients by ions and photons are 0.2 and 0.01, respectively. The skin is initially uncharged and the DBD voltage is −25, −30 or −40 kV. The voltage rise time is 0.1 ns and the voltage was kept constant during the time the plasma portion of the simulation was conducted, which is 1 ns. These voltages were chosen to span the voltages that are typically used in DBDs in plasma medicine [11, 12]. The partial differential equations for all species (charged and neutral), electron temperature and electric potential are integrated for the duration of the discharge pulse. After that time, Poisson's equations and continuity equations for charges species are no longer integrated and only the densities of neutral species and photons are computed.

Table 2. Permittivities and conductivities used in the model [52, 53].

	Dead Cells	Cell membrane	Cytoplasm	Nucleus
$\varepsilon/\varepsilon_0$	3	5.8	30	20
σ (Ω^{-1} cm^{-1})	10^{-8}	8.7×10^{-8}	4.8×10^{-3}	3.0×10^{-5}

The filament evolution is discussed during the 'plasma time' (1 ns) which includes crossing the gap between the upper dielectric and the thumb and spreading of the plasma over the thumb surface. Radicals produced during the plasma time then diffuse and react in the gap for 0.5 ms ('diffusion time'). The diffusion time corresponds to the intra-pulse period a DBD operating at the nominal frequency of 2 kHz. We investigated with this high level of detail only the first discharge pulse (and in one case, the 500th pulse). The actual treatment of tissue occurs using multi-kHz plasmas for seconds or minutes. Traylor *et al* [50] have shown that in the absence of forced gas flow there is accumulation and evolution of ROS and RNS species over periods of up to hundreds of seconds. To contrast the fluxes of radicals and ions produced by single pulses (albeit with spatial detail) with those generated by a long sequence of pulses and afterglow periods, global modelling was also performed.

The global modelling platform, Globlal_Kin, is essentially the same as described in [51] and so will be only briefly described here. Global_Kin consists of a time integration of rate equations for the densities of charged and neutral species, electron and gas temperature, surface chemistry and circuit quantities. The rate equations for the density of gas phase species include electron impact, ion–molecule and neutral chemistry reactions, and change in densities due to transport to and reaction on surfaces. Transport consists of diffusion to surfaces (either neutral or ambipolar for charged species), reactions on the surface and a return flux of reaction products. The surface model consists of a surface-site-balance formulation. For this application, the circuit model consists of a resistor whose value is given by the volume averaged resistivity of the plasma and the shape of the plasma, a series capacitance representing the bounding dielectrics, a series inductance representing the physical inductance of the device and a parallel storage capacitor that is charged to a specified line voltage. The reaction mechanism we used for humid air is essentially the same full mechanism described in detail in [48].

The combined rate equations are simultaneously integrated forward in time. The initial conditions for the first

pulse is a charge neutral plasma density of 10^8 cm^{-3}. A switch is closed between the storage capacitor and the inductor and voltage flows onto the reactor. The full set of rate equations are integrated until the voltage across the gap is below self-sustaining due to charging of the dielectrics. At that time, the circuit equations are no longer integrated and the remaining equations continue to be integrated until the next voltage pulse is applied based on the specified pulse repetition frequency (PRF). At that time, the storage capacitor is recharged to the line voltage, the switch is closed and the process is repeated for a specified number of pulses.

3. DBD filament directly over the wound

The electron and charge density for −40 kV applied voltage when the plasma filament is located directly over the wound are shown in figure 2. The electric field and electron temperature are shown in figure 3. Within 0.4 ns after initiation of the streamer at the dielectric, the plasma filament reaches the skin. Upon intersecting the skin, the filament charges the surface, producing lateral electric fields which spread the filament over the tissue to two-three times its diameter in the gas phase. Electron densities reach (1–3) × 10^{15} cm^{-3}, increasing near the surface due to the large capacitance of the exposed features which enables a larger current density. The negative space charge, $-\rho$, defines the boundary of the head of the filament during propagation across the gap. When the filament strikes the skin's surface, charging of the surface results in the plasma following the topography of the surface. The uncharged skin ahead of the surface hugging plasma produces a potential difference with the head of the streamer, which provides the electric field to advance the discharge along the surface. As the streamer spreads to those points, charging the capacitance of the surface, the avalanching electric field is advanced towards uncharged skin. This process is similar to the spreading of a filament on a conventional dielectric with the exception that the skin surface and wound are not flat [54]. The filament reorients itself to arrive normal to the surface. This reorientation is due to the electric field that becomes more normal to a surface that has finite conductivity.

For a single filament that is not limited by surface charges produced by neighboring filaments or remnant charges on the surface from prior pulses, spreading on the surface can be many times its diameter upon intersection with the skin. Electric fields reach 280–370 kV cm^{-1} at the head of the surface resident streamer, resulting in a high electron temperatures up to 15 eV in the streamer head along the surface.

The densities of O, OH and NO are shown in figure 4 at the time the streamer intersects the skin and has started to spread (0.5 ns), and 0.5 ms after the discharge pulse. O atoms are dominantly produced by direct electron impact dissociation and dissociative attachment to O_2 and by excitation transfer from $N_2(A)$ to O_2. O atoms are dominantly consumed by formation of O_3. OH is dominantly formed by electron impact dissociation of H_2O and consumed by formation of H_2O_2. NO is not directly produced by electron impact. At ambient temperatures and on these time scales, NO is produced

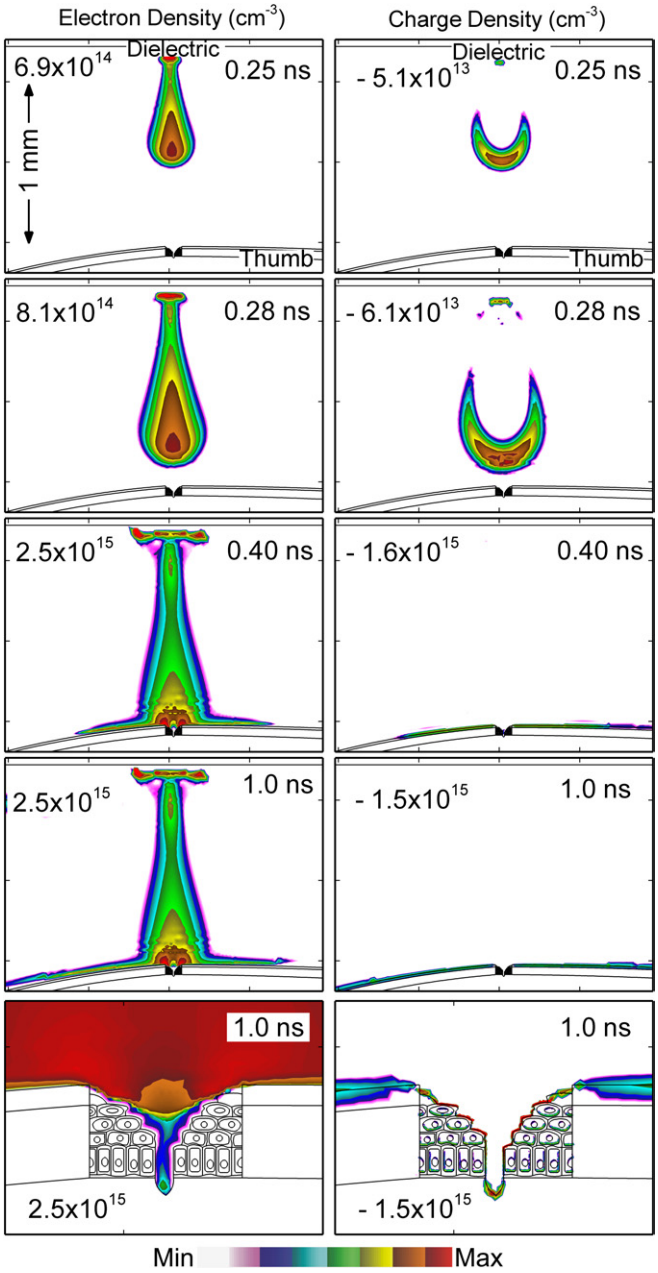

Figure 2. Time evolution the electron density (left column) and space charge (right column) for a plasma filament located over the wound. The electron density reaches 2.5 × 10^{15} cm^{-3}. The plasma spread is 3–5 filament widths. Charge is deposited on the thumb surface and penetrates into the wound. The bottom row shows a close-up of electron density and charge. Conditions are humid air ($N_2/O_2/H_2O$ = 79/20/1) and −40 kV. The maximum magnitude is indicated in each frame.

dominantly by

$$N^* + O_2 \rightarrow NO + O, \qquad k = 6.8 \times 10^{-12}\ \text{cm}^3\ \text{s}^{-1}$$
$$N + OH \rightarrow NO + H, \qquad k = 2.9 \times 10^{-11}\ \text{cm}^3\ \text{s}^{-1}$$
$$N^+ + O_2 \rightarrow NO + O^+, \qquad k = 3.6 \times 10^{-11}\ \text{cm}^3\ \text{s}^{-1}$$

where k is the room temperature rate coefficient.

The initial density of 3.9 × 10^{15} cm^{-3} for O atoms produced in the gap during the discharge pulse is diminished to 5.1 × 10^{11} cm^{-3} by the formation of O_3 after 0.5 ms. In

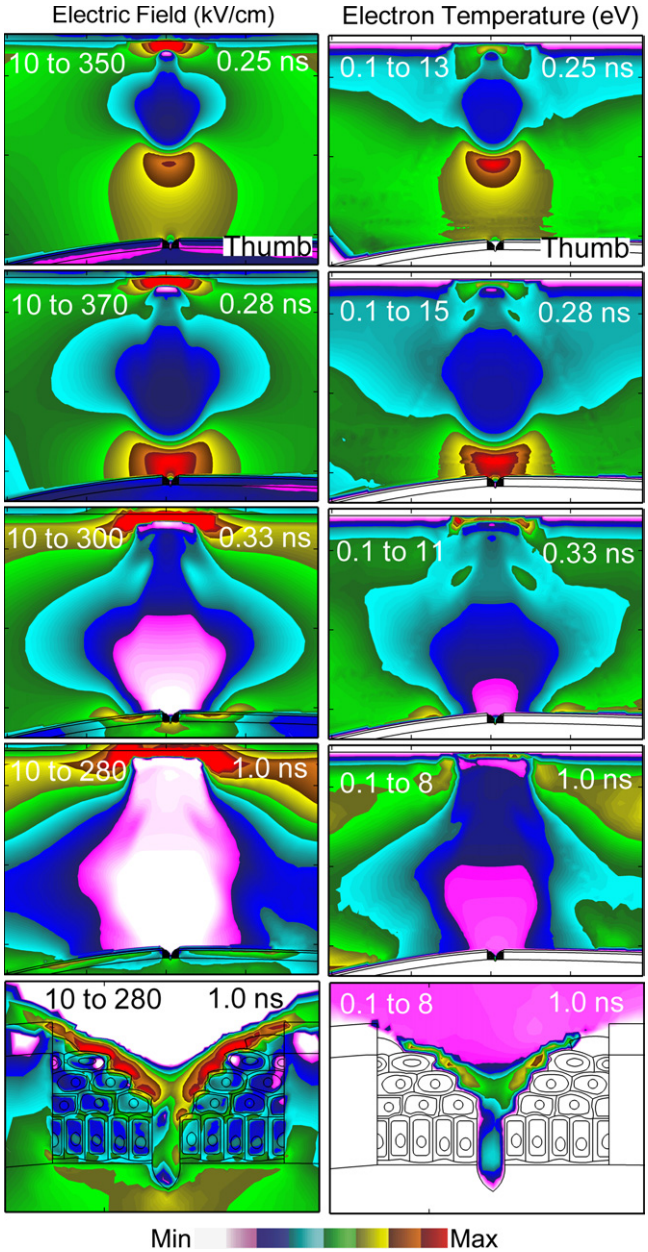

Figure 3. Time evolution of electric field (left column) and electron temperature (right column) for plasma filaments located over the wound. The electric field directly penetrates into the wound reaching 280–370 kV cm^{-1} resulting in a high (up to 15 eV) electron temperature in the streamer head. The bottom row shows a close-up. Conditions are humid air ($N_2/O_2/H_2O = 79/20/1$) and -40 kV. The range of values plotted is indicated in each frame.

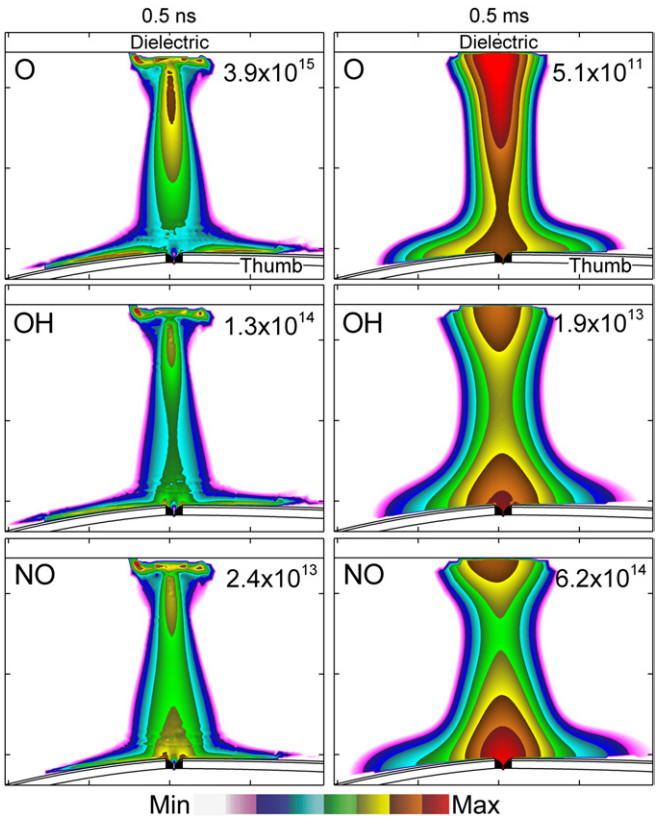

Figure 4. Comparison of (left column) short term 0.5 ns and (right column) long term 0.5 ms densities for O, OH and NO for the plasma filament over the wound. Radicals are mainly produced by electron impact in the head of the filament. Conditions are humid air ($N_2/O_2/H_2O = 79/20/1$) and -40 kV. The maximum value plotted is indicated in each frame. The values are plotted over a 2-decades log-scale.

ambient temperature air and in the absence of hydrocarbons, OH is relatively unreactive, other than forming H_2O_2, and so simply diffuses during the afterglow having an initial density of 1.3×10^{14} cm^{-3} and diminishing to 1.9×10^{13} cm^{-3}, albeit over a larger volume. NO increases its density from a peak of 2.4×10^{13} cm^{-3} during the discharge pulse to 6.2×10^{14} cm^{-3} after 0.5 ms. However, its total inventory increases by significantly larger proportion as the volume occupied by NO also increases.

Plasma properties near and inside the wound on the plasma time scale of 1 ns are shown in figure 5 (electron density, electric field, electron temperature, $[O_2^+]$, $-\rho$, and electron impact ionization source S_e). Selected densities (O, OH, O_2^-, O_3, NO and O^-) are shown in figure 6. These densities correspond to the filament being directly over the wound for the last time frame of figure 2. For the plasma density and electron temperature adjacent to the surface of the wound, the Debye length is of the order of 1 μm, which allows the plasma to conformally cover the wound and penetrate inside the smallest spaces in the wound. The peak in electron density is 1.1×10^{15} cm^{-3} on the surface of the wound and 2×10^{13} cm^{-3} deep inside the wound. Charging of the surfaces of the cells produces transient electric fields of up to 380 kV cm^{-1}. These electric fields can lead to electroporation and be an additional factor in wound healing. The electron impact source peaks at 5×10^{21} cm^{-3} s^{-1} indicating that ionization also takes place inside the wound, though on a transient basis. As a result, the electron temperature can peak up to 6 eV deep inside the wound resulting in plasma production in close contact with cells.

Electron impact dissociation adjacent to and inside the wound produces radicals in close contact with the cells on short time scales. On the plasma time scale of 1 ns, these radicals (and their densities) include O (7×10^{14} cm^{-3}), OH (3.1×10^{13} cm^{-3}) and NO (2.2×10^{13} cm^{-3}). Three body attachment of electrons to O_2 produces antimicrobial active

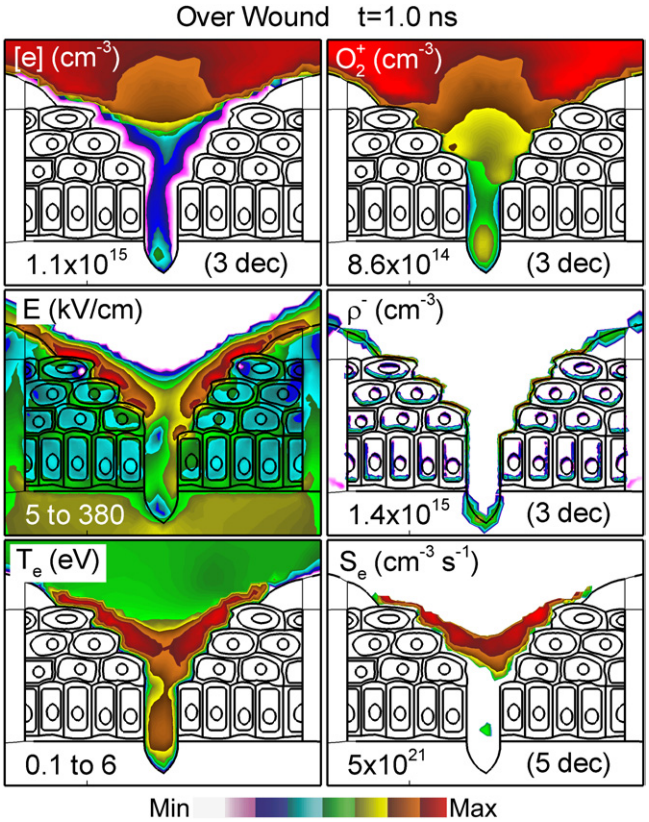

Figure 5. Plasma properties inside the wound at 1.0 ns for electron density, O_2^+ density, electric field, negative charge density, electron temperature and electron impact source function. The small plasma Debye length of the order of 1 μm allows electrons and ions to penetrate inside the wound. The electric field is enhanced near the cells resulting in high electron temperatures. Charge accumulates on the membranes resulting in high potential drop across the cells' membranes. Conditions are humid air ($N_2/O_2/H_2O = 79/20/1$) and -40 kV. The maximum value plotted is indicated in each frame. The number of decades plotted are indicated for log-scale plots.

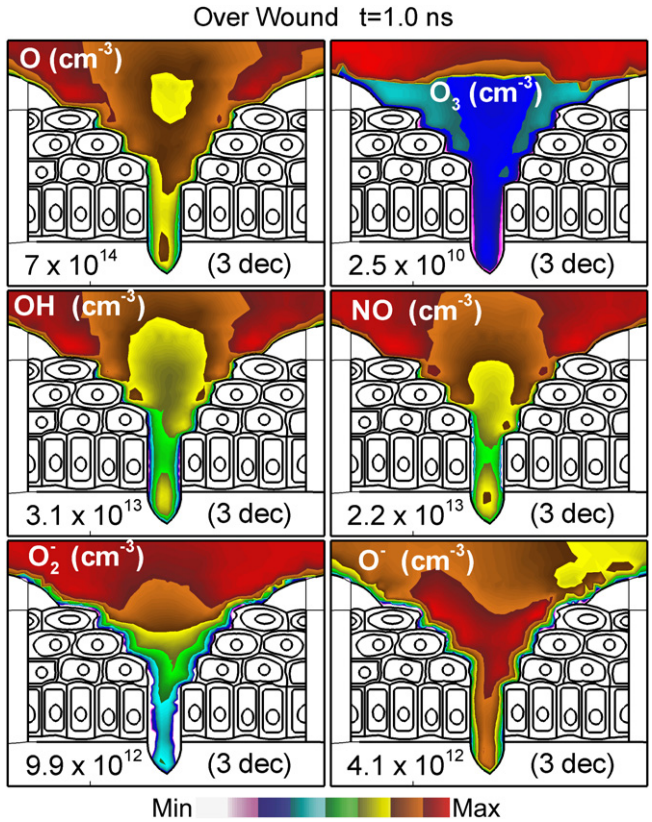

Figure 6. Radical and ion densities inside the wound at 1.0 ns for O, OH, O_2^-, O_3, NO and O^-. The maximum value plotted is indicated in each frame. Conditions are humid air ($N_2/O_2/H_2O = 79/20/1$) and -40 kV. The number of decades plotted are indicated for log-scale plots.

species such as O_2^- (9.9×10^{12} cm^{-3}) with similar densities. During the plasma time scale, production of O_3 and H_2O_2 is small. The rate coefficient for O_3 formation is approximately 5×10^{-34} cm^6 s^{-1}. So even in atmospheric-pressure air, the conversion of O to O_3 requires tens of μs. The production of O_3 and H_2O_2 occurs over the longer interpulse period. The UV photon producing state, N_2^{**}, has densities in excess of 5×10^{14} cm^{-3} adjacent to the wound, thereby providing a nearby source of UV photons. On this short time scale, the locations of radicals largely reflect the location of their creation by either electron impact (O radicals) or reactions of radicals with feedstock gases (nitric oxide NO). These locations also reflect the path of the streamer as it spreads along the surface and enters the wound. During the time between discharge pulses, diffusion will spatially homogenize these initial densities. As such, the largest densities of some radicals occur inside the wound because that is where they were initially produced. These radicals then diffuse out of the wound. Other radicals are initially produced mostly outside the wound, and diffuse into the wound.

Although densities are informative measures of the production of radicals, the fluxes to surfaces determine the treatment potential. The fluxes and fluence (time integrated fluxes over the plasma time scale) of ions and photons to the surface are shown in figures 7 and 8. Fluxes and fluences are shown along the surface of the wound from location A to F (indicated in figure 1(*c*)) for an applied voltage of -40 kV. Although the flux of negative ions is small compared to that of the positive ions, the flux does peak in the smallest portion of the wound. This is likely a consequence of the time averaged electron temperature in that small space being low, a condition which will preferentially produce negative ions compared to positive ions. (The electron temperature can spike but on the average it is low.) The electric field at that location is relatively small due to the partial shielding from charge deposited at higher locations.

The fluence is perhaps the better criterion for determining the possible importance of a given species. For example, the typical size of a cell is a few micrometres, producing a surface area exposed to the plasma of 4–5 μm^2. Therefore the fluence during a single pulse should exceed 10^7 cm^{-2} in order for each cell to receive at least one of the incident species during a single pulse. For a DBD repetition rate of 2 kHz, every surface site (roughly 5×10^{14} sites cm^{-2}) will receive one ion, radical or photon during 4–5 s of treatment if the fluence per pulse is at least 5×10^{10} cm^{-2}. Rating the importance of radical fluxes is ultimately measured by the product of the fluence and reaction probability. However for the purposes

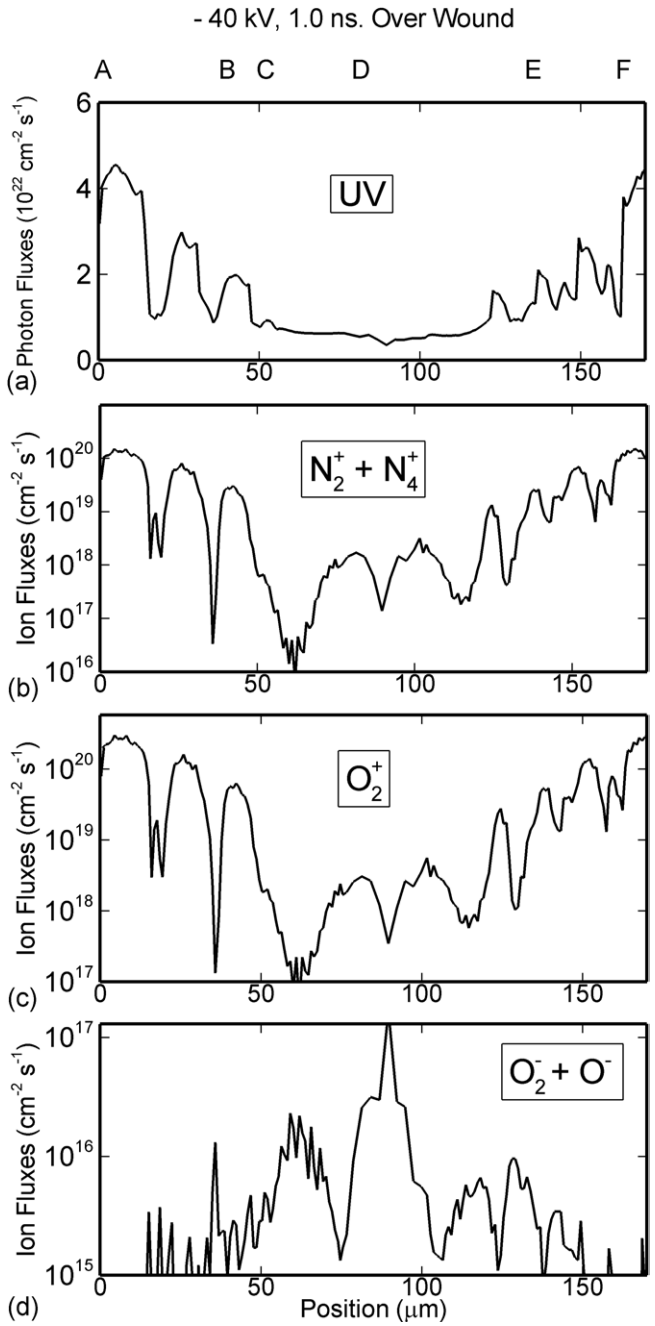

Figure 7. Instantaneous UV and ion fluxes recorded at 1.0 ns for the plasma filament over the wound. (*a*) Photon fluxes; (*b*) sum of N_2^+ and N_4^+, (*c*) O_2^+, and (*d*) sum O^- and O_2^- fluxes. Fluxes are recorded along the surface A to F as indicated in figure 1(*c*). Fluxes reflect the cell topography with large fluxes arriving to the top of the cells having large view angles to the plasma and shadowing of fluxes in between the cells. Conditions are humid air ($N_2/O_2/H_2O = 79/20/1$) and −40 kV.

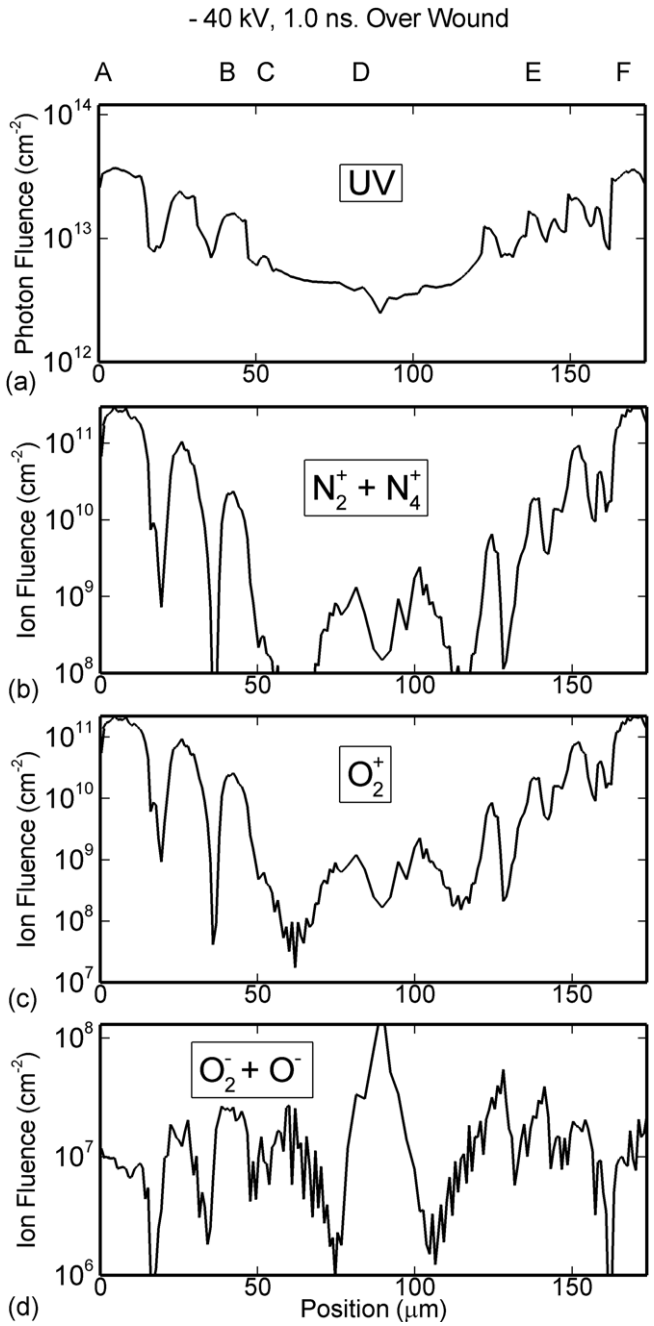

Figure 8. UV and ion fluences over the plasma time of 1.0 ns. (*a*) Photon fluxes; (*b*) sum of N_2^+ and N_4^+ (*c*) O_2^+, and (*d*) sum of O^- and O_2^- fluxes. Fluences are recorded along the surface A to F indicated in figure 1(*c*). During the short plasma time fluences still reflect the cell pattern. Conditions are humid air ($N_2/O_2/H_2O = 79/20/1$) and −40 kV.

of discussion, important fluxes are indicated by fluences that result in a cell receiving at least tens of that species during a single pulse and its interpulse period (fluence/pulse exceeding 5×10^8 cm^{-2}). This fluence results in a few per cent to 10% of the surface sites on the cell receiving the incident species during a 10 s treatment at a DBD repetition rate of a few to 10 kHz, parameters that are typical for treatment of wounds.

Photon fluxes in excess of $(1–4)\times10^{22}$ cm^{-2} s^{-1} are incident onto the wound with photon fluences of 10^{12}–10^{13} cm^{-2} per pulse. This corresponds to each surface site on the cell receiving 0.01–1 photon s^{-1} at 10 kHz. The photon fluxes reflects the topography of the cells. Large fluxes of photons arrive onto the horizontal surfaces of cells and shadowing occurs in between the cells or by cells blocking the line of site to the plasma. Photons can arrive from the surface originating from many tens or hundreds of micrometres away, thereby smoothing the distribution of photon fluxes.

The delivery of ion fluxes is determined by more local effects as the mean free paths of ions at atmospheric pressure are at best a few micrometres and the ions respond to surface charging. The charges deposit on the protruding features of the wound which results in enhancement of the electric fields near those features and depletion of the electric fields in the shadowed region between the cells. The end result is that ions are focused onto the protruding features of the wound having large view angles to the plasma. Over the duration of the ns pulse, ions cannot transit from remote locations and so ions arrive at surfaces from only a few micrometres of the surface. This contrasts with photons that can arrive from much further locations. The cells on the top of the wound (sites A, B, E, F) receive hundreds to thousands of positive ions during the pulse (fluence of 10^{10}–10^{11} cm^{-2}/pulse) corresponding to each site receiving at 1–10 ions during a 10 s treatment, though few ions penetrate deeply within the wound. The positive ion fluences on this short time scale are dominated by N_2^+, N_4^+, and O_2^+. Negative ion fluxes and fluences (O_2^-, O^-) are smaller than those of the positive ions by a factor of 10^3–10^4. Note that unlike the ion fluxes which basically terminate at the end of the pulse, there is still production of UV fluxes during the interpulse period due to the finite lifetime of the radiating states.

The maximum charge densities produced on the surface of the cells are approximately 2×10^{-8} C cm^{-2}. This corresponds to a momentray electrostatic pressure on the cell membrane of approximately 2×10^6 N m^{-2}. Although this is well below the tensile strength (or rupture strength) of many strains of cells and bacteria [55], it is known that such mechanical stresses can produce physiological responses in cells, which affects their growth, differentiation and apoptosis [56].

Instantaneous ROS fluxes to the wound recorded at 1.0 ns are shown in figure 9 and fluences integrated over the discharge pulse are shown in figure 10. On the short (plasma) time scale ROS fluxes and fluences reflect the view angles and shadowing of the surface of cells similarly to that for the ions. The location of electron impact dissociation producing these fluxes are modulated by the electric field enhancement that occurs by surface charging. However the modulation in the neutral fluxes across the cell surfaces is less severe than that for ions since neutral species are not directly affected by intensification of electric fields at cell edges. (Ion drag forces between ions and neutrals are included in the model but these momentum transfer processes are not important.) Directly produced primary ROS (including O, $O_2(^1\Delta)$, OH) have fluxes in excess of 10^{15}–10^{18} cm^{-2} s^{-1} whereas ROS resulting from secondary reactions, such as O_3, have small fluxes on this time scale. The RNS fluxes and fluences on these times scales are small with the exception of N_2^* which is produced by direct electron impact.

The filamentary nature of the DBD discharge does certainly have an influence on the ion and photon fluxes to the cell surfaces, and on the production of ROS and RNS. However, the non-uniform production of ROS and RNS is significantly mediated by diffusion during the interpulse surface. For example, the densities of ROS and RNS in the vicinity of the wound after 0.5 ms are shown in figure 11. The fluxes and

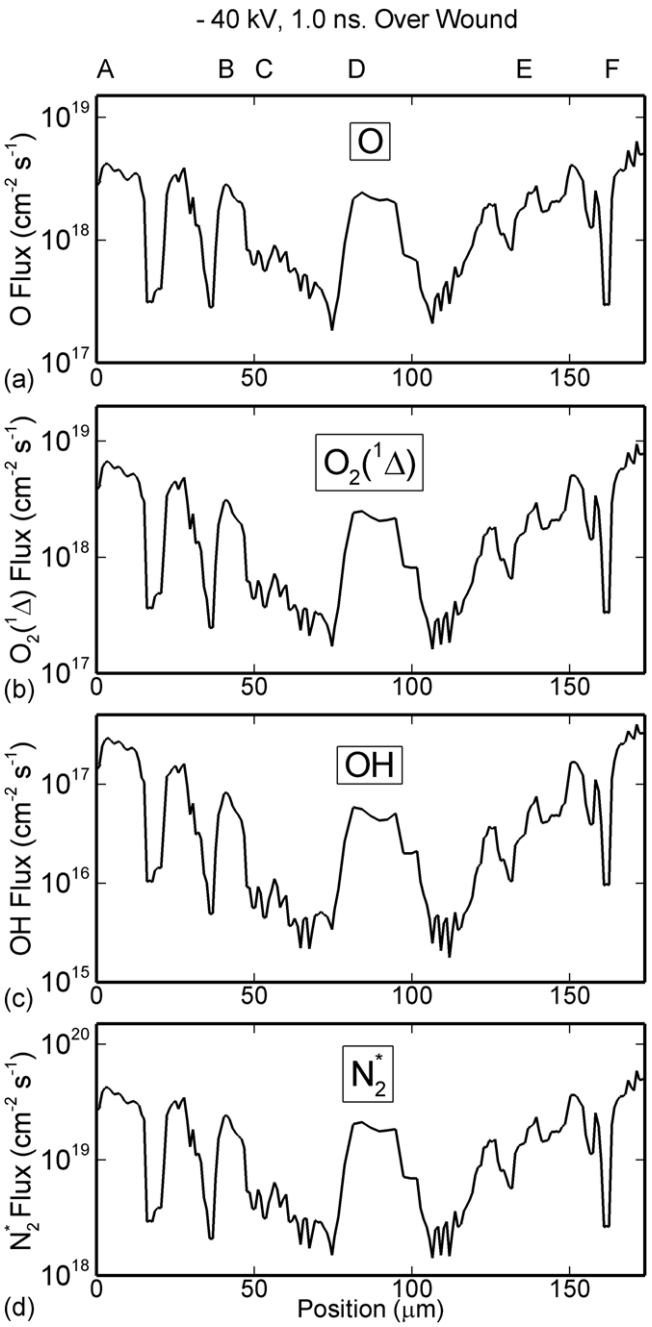

Figure 9. Instantaneous fluxes recorded at 1.0 ns. (*a*) O, (*b*) $O_2(^1\Delta)$, (*c*) OH and (*d*) N_2^* . Fluxes are recorded along the surface A to F indicated in figure 1(*c*). On the short plasma time scale fluxes reflect cell patterns due to their production by electron impact. Conditions are humid air ($N_2/O_2/H_2O$ = 79/20/1) and −40 kV.

fluences of ROS to the wound at 0.5 ms are shown in figure 12 for voltages of −25, −30 kV, and −40 kV. The densities of all ROS and RNS in the vicinity of the wound are essentially uniform due to the redistribution of their initially non-uniform sources by diffusion. (Note the narrow dynamic range of values plotted in figure 11.) This contrasts with the many decades of non-uniformity for the short term radical exposure shown in figures 9 and 10. Note that on these longer time scales radicals can appear to either diffuse into or out of the wound. This is typically not a result of radical production inside the

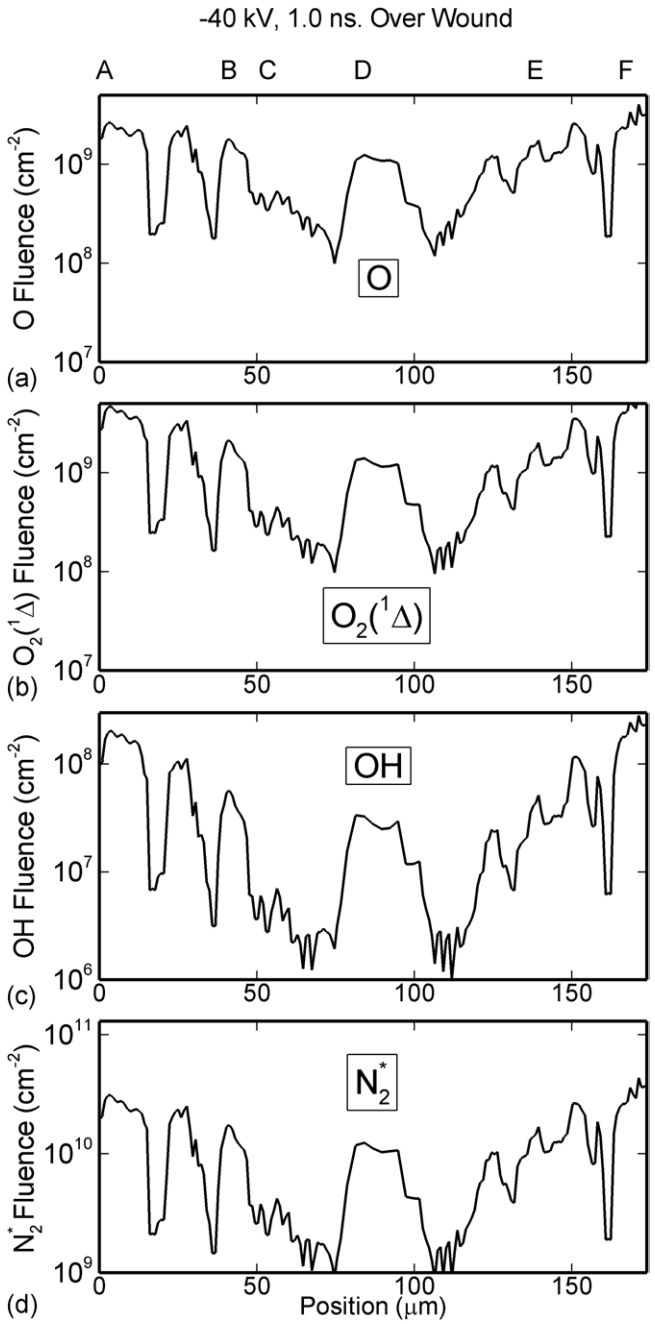

Figure 10. Fluences over the plasma time 1.0 ns. (*a*) O, (*b*) $O_2(^1\Delta)$, (*c*) OH and (*d*) N_2^*. Fluences are recorded along the surface A to F indicated in figure 1(*c*). Conditions are humid air ($N_2/O_2/H_2O = 79/20/1$) and −40 kV.

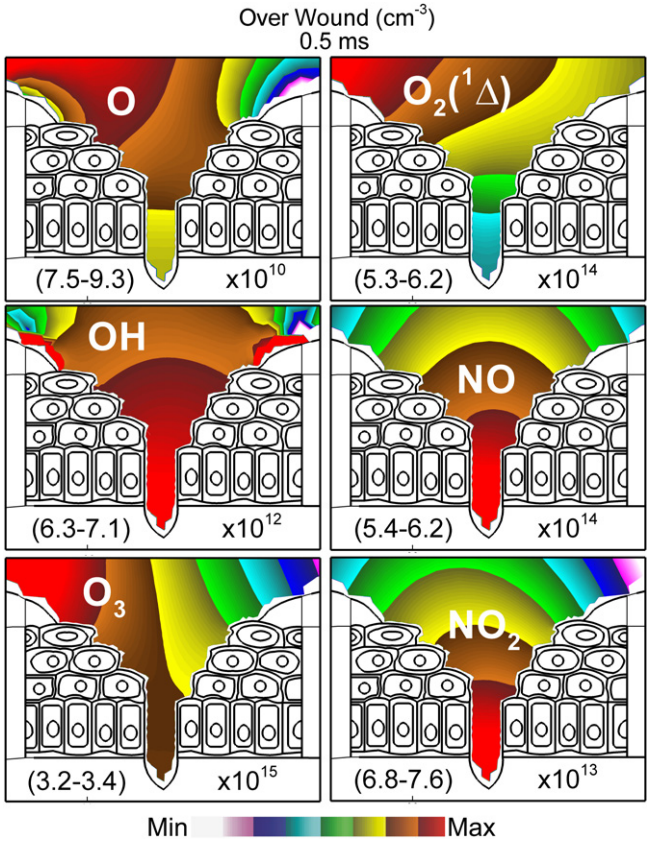

Figure 11. ROS and RNS inside the wound at 0.5 ms. During the millisecond time scale radicals can diffuse into as well as out of the wound. Long-term diffusion redistributes radicals more uniformly than their sources. Conditions are humid air ($N_2/O_2/H_2O = 79/20/1$) and −40 kV. The range of values plotted is indicated in each frame. Note the narrow dynamic range plotted.

wound but rather is a result of more rapid depletion of these radicals by reactions outside the wound.

In all cases, fluxes and fluences increase with increasing magnitude of the voltage, increasing by a factor of 2–3 from −25 kV to −40 kV. This increase with voltage is smaller than what one would expect based only on the increase in stored energy in the capacitor which scales with voltage-squared. We partly attribute this lower than expected increase in fluxes and fluence to the fact that the majority of the increase in energy is expended in spreading of the streamer on the surface, and so does not strongly affect the fluxes directly beneath the streamer.

On the scale of the wound, the fluxes and fluences are essentially uniform with the exception of O atoms. ROS that are directly produced by electron impact processes (e.g., $O_2(^1\Delta)$, OH) have fluxes in excess of 10^{17}–10^{18} cm^{-2} s^{-1}. The fluences per pulse are in excess of 10^{15} cm^{-2} for $O_2(^1\Delta)$ and 10^{14} cm^{-2} for OH. These fluences, at a DBD repetition rate of 10 kHz, produce many thousands of ROS molecules to each site on the cell per second. The reactivity of these species on the cell appear not to be limited by the availability of flux but rather are limited by the probability of reaction. The fluxes of O atoms at 0.5 ms are 2–3 orders of magnitude smaller than $O_2(^1\Delta)$ and OH, whereas the fluences are within a factor of 10 of $O_2(^1\Delta)$ and OH. The small instantaneous flux and large fluence results from the O atoms being consumed during the interpulse period in large part to form O_3. Nevertheless, for a PRF of 10 kHz, each site on the cell receives hundreds to thousands of O atoms. Note that the O atom fluence is depressed within the wound. This results from conversion of O to O_3. The O atoms within the small wound consumed in this manner are not replenished from the larger reservoir of O atoms outside the wound as this supply is itself depleted as it diffuses into the wound.

The secondarily produced ROS O_3 has a fluence in excess of 10^{16} cm^{-2} yet an instantaneous flux after 0.5 ms in excess of 10^{19} cm^{-2} s^{-1}. O_3 is relatively unreactive in the gas phase and so its density (flux and fluence) will accumulate over

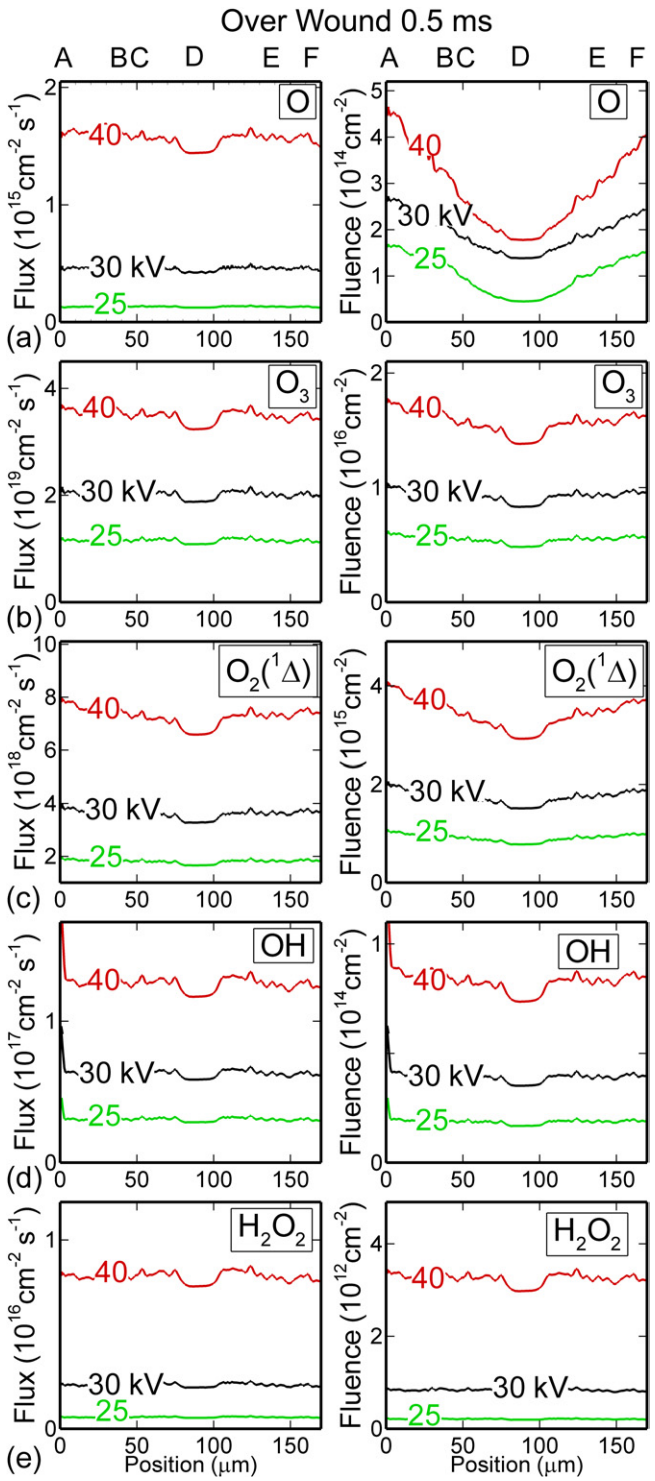

Figure 12. ROS fluxes (left column) and fluences (right column) at 0.5 ms arriving to the wound along the A to F surface (see figure 1(*c*)) for a plasma filament over the wound for applied voltages of −25, −30 and −40 kV. (*a*) O, (*b*) O_3, (*c*) $O_2(^1\Delta)$, (*d*) OH and (*e*) H_2O_2. By 0.5 ms diffusion nearly uniformly redistributes radical fluxes over the wound surface, though slight depletion of radicals at the bottom of the wound is still traceable. (Note the narrow dynamic range of the plots.) Fluences are less uniform (especially for atomic oxygen) as they reflect the history of radical diffusion into and out of the wound. Conditions are humid air ($N_2/O_2/H_2O$ = 79/20/1).

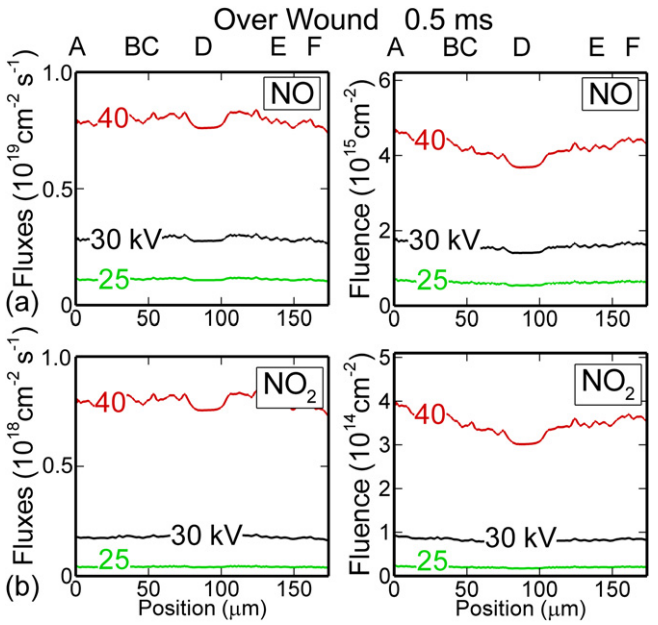

Figure 13. RNS fluxes (left column) and fluences (right column) at 0.5 ms arriving to the wound along the A to F surface (see figure 1(*c*)) for a plasma filament over the wound for applied voltages of −25, −30 and −40 kV. (*a*) NO flux; (*b*) NO_2. Conditions are humid air ($N_2/O_2/H_2O$ = 79/20/1).

many hundreds to thousands of pulses, as shown by the global modelling discussed below. Similarly, H_2O_2 has a significant instantaneous flux to the wound (10^{16} cm^{-2} s^{-1}) yet a small fluence, (10^{12}–10^{13} cm^{-2}). H_2O_2 is dominantly produced through the bi-radical reaction OH + OH + M → H_2O_2 + M. H_2O_2 is also relatively uncreative in low humidity air and so will accumulate over many hundreds to thousands of pulses. [27]. So these fluxes and fluences are lower limits to what is expected with DBDs having high PRF.

Long-term (0.5 ms) instantaneous fluxes and fluences for RNS are shown in figure 13. There are no specific differences between the behaviour of fluxes and fluences of RNS compared to ROS. Due to the cyclic conversion of NO to NO_2 and reverse reactions of NO_2 to NO, high fluxes of both NO and NO_2 in excess of 10^{18}–10^{19} cm^{-2} s^{-1} are produced, with fluences of 10^{15}–10^{16} cm^{-2} for NO and 10^{14}–10^{15} cm^{-2} for NO_2. Even without accumulation over multiple pulses, these values correspond to many thousands of RNS to each surface site for each second of treatment at a PRF of many kHz.

4. Filaments to the left and right of the wound

The filaments in DBDs are often randomly generated and their landing points on the substrate are also somewhat random. Having said that, it is true that DBDs can display self-organization wherein their two-dimensional spatial distribution is fairly constant, a consequence of space charge forces between the filaments and charging on the surface [57, 58]. This self-organization may be less important in the context of plasma medicine where there will likely be intentional motion of the applicator by the physician during treatment.

In the absence or presence of self-organization, the position of the wound with respect to the landing-site of the plasma filament is not particularly critical for treatment for at least three reasons. First, in the absence of self-organization, the filaments in DBDs are statistically distributed in space and the probability that a small wound is intersected by one or another filament is rather high. For large wounds, the same argument provides for fairly uniform coverage as there is high likelihood for filaments to arrive on the wound. Second, in the case of self-organized DBD structures, the spreading of filament on the surface will in large part cover the surface. Third, the post-pulse diffusion of radicals tends to homogenize the fluxes of radicals to surfaces and so the precise position that the filament strikes the skin relative to the wound is not critical. As a demonstration of these trends, we will discuss fluxes to surfaces when the filament strikes to the left and right of the wound.

Electron densities for filaments striking to the left and right of the wound are shown in figure 14. Electric field, charge density and radical densities within the wound on the plasma time scale are shown in figure 15. When the plasma filament strikes the skin surface, charging of the surface produces lateral electric fields that result in the spreading of the filament on the surface. The plasma spreads over 3–5 filament widths, a value that ultimately depends on the capacitance of the surface and the charging voltage. As the filament spreads on the surface, it penetrates into the wound with densities commensurate with filaments striking directly onto the wound. In this particular case, the skin curves downward to the left and so the filament to the left of the wound qualitatively differs from that to the right. The filament to the left has curvature that aligns the filament to the normal to the surface. However, the peak plasma densities and temperatures are nearly the same in both cases.

As the filament plasma spreads on the surface it follows the topography of the tissue as long as the Debye length is shorter or commensurate than the features the filament spreads onto (or into). The plasma spreads on the surface by charging the surface which generates components of electric field parallel to the surface. These parallel components of the electric field then serve to propagate the filament along the surface. As the filament spreads on the surface of the skin and approaches the open wound, parallel components of the electric field continue to direct the filament across the wound, as though launching a small streamer from the side of the wound. This streamer then strikes the opposite side of the wound, which charges that surface and produces electric components which oppose the spreading of the filament along the surface. Depending on the details of the surface topography and capacitance of the wound, the wound may stop spreading of the filament on the surface, as shown in figure 14. These trends result in some asymmetry of the charging of the cells within the wound and some asymmetry in the initial production of ROS and RNS, as shown in figure 15. Charging of cells is the highest on the side of the wound opposite the entry point of the spreading filament.

When the filament is directly over the wound (see figure 5), the plasma is essentially symmetric but concentrated at the top of the wound where the view angle to the plasma is largest.

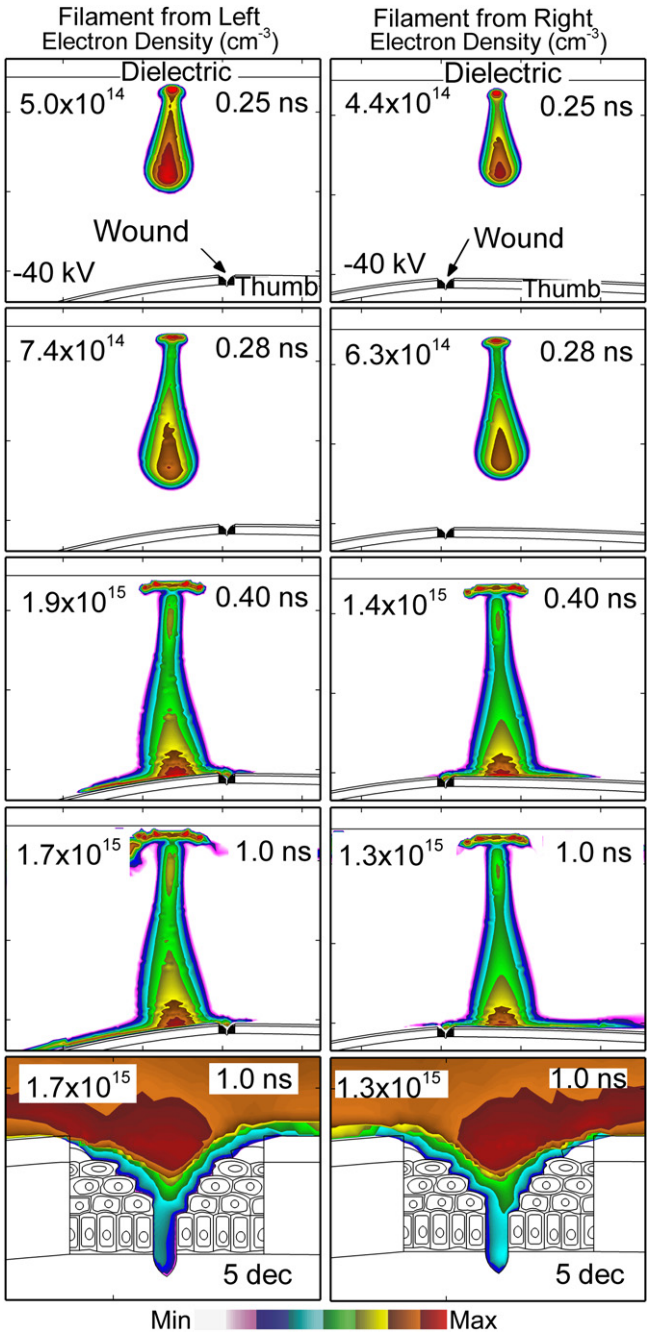

Figure 14. Time evolution of the electron density for filaments striking (left column) to the left of the wound and (right column) to the right of the wound. The plasma spreads over 3–5 filament widths and penetrates into the wound. The bottom row shows a close-up of the electron density in the wound. Conditions are humid air ($N_2/O_2/H_2O = 79/20/1$) and −40 kV. The maximum magnitude is indicated in each frame.

For the filament spreading into the wound from one side, the surface with the largest view-angle to the plasma is that opposite the incoming surface discharge. This surface with the largest view angle receives the largest charge, which produces the larger electric field on the surface. The densities of ROS and RNS initially produced in the wound on the plasma time scale are 4.2×10^{13} cm^{-3} for OH, 1.9×10^{15} cm^{-3} for O radicals, and 1.7×10^{12} cm^{-3} for NO, comparable to that produced when the filament is directly over the wound. These densities are

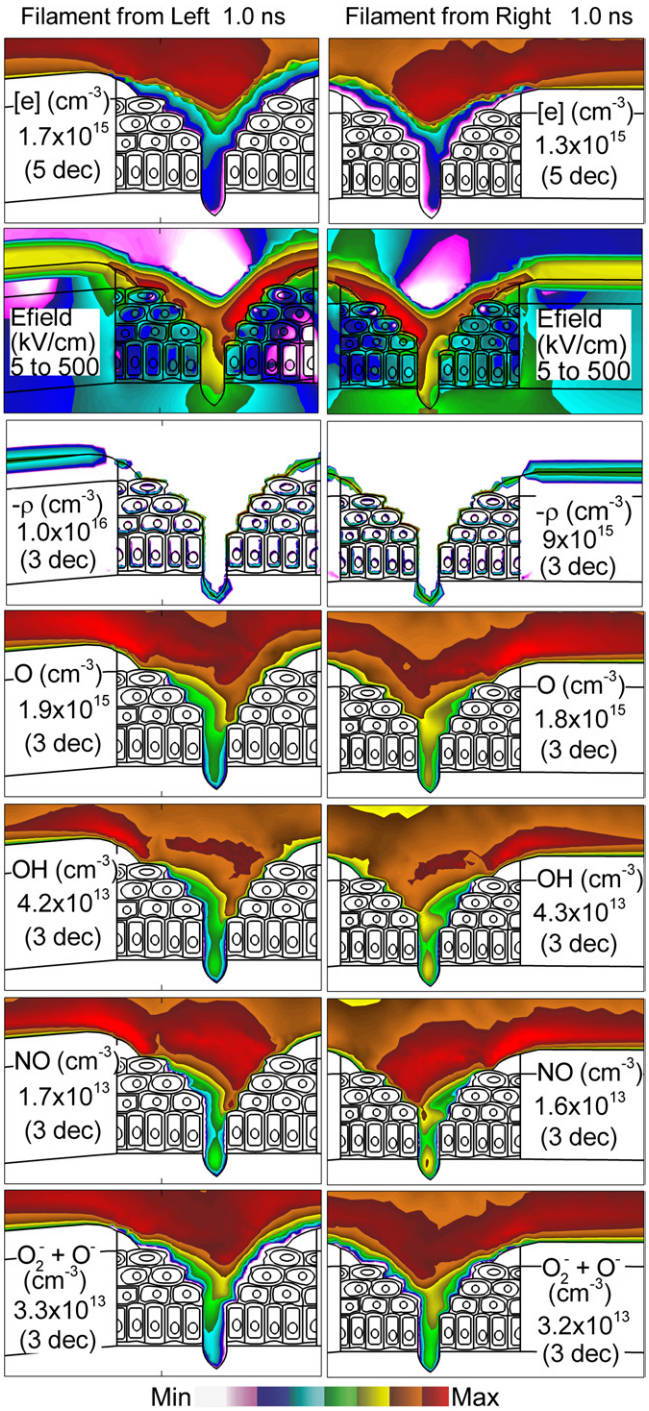

Figure 15. Plasma parameters inside the wound for a plasma filament striking (left column) to the left and (right column) to the right (right column) of the wound recorded at 1.0 ns. From top to bottom—electron density, electric field, negative charge density, O, OH, NO and sum of O_2^- and O^-. The charged particle densities and electric fields are largest on the opposite side of the wound from where the plasma enters. Conditions are humid air ($N_2/O_2/H_2O$ = 79/20/1) and −40 kV. The maximum value plotted is indicated in each frame and the number of decades plotted are indicated for log-scale plots.

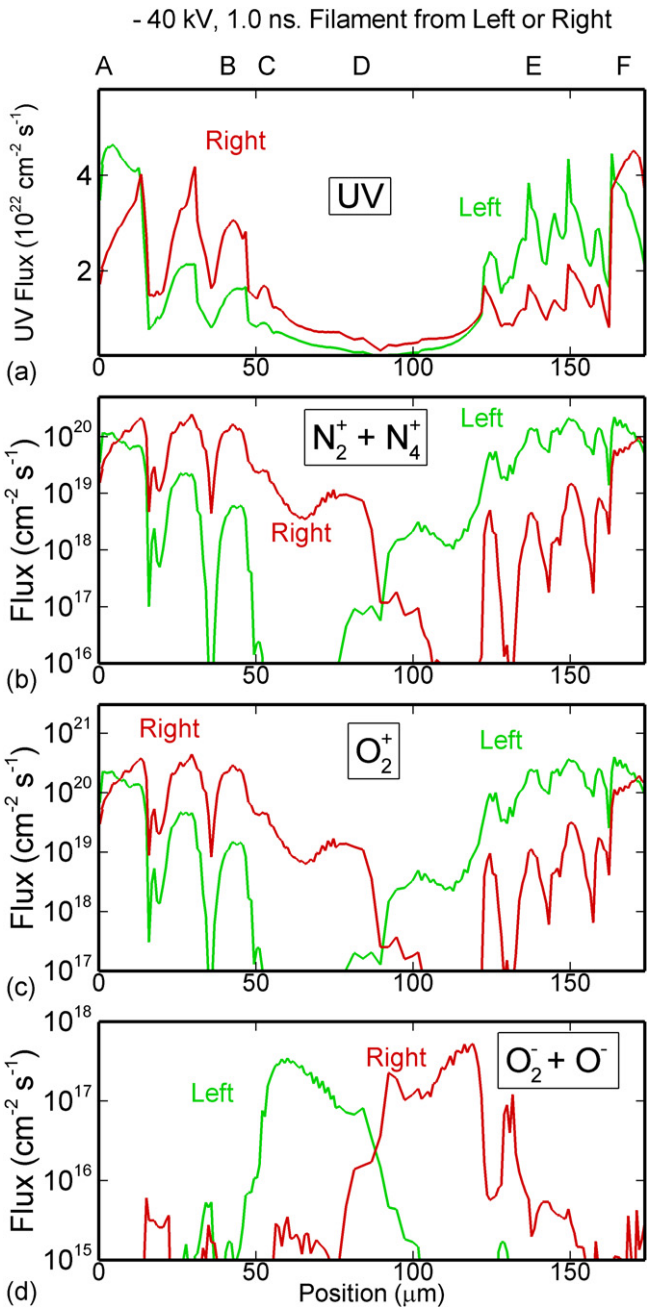

Figure 16. UV and ion fluxes recorded at 1.0 ns for plasma filaments striking to the left (green curve) and to the right (red curve) of the wound. (*a*) UV photon flux (*b*) sum of N_2^+ and N_4^+ (*c*) O_2^+, and (*e*) sum of O^- and O_2^- fluxes. Fluxes are recorded along the A to F surface (see figure 1(*c*)). Conditions are humid air ($N_2/O_2/H_2O$ = 79/20/1) and −40 kV.

initially asymmetrically distributed in the wound, which is a direct reflection of the initial plasma densities.

The UV and ion fluxes and fluences into the wound on the plasma time scale are shown in figures 16 and 17. The delivery of ions to the cell surfaces are sensitive to the initial location of the filament. When the filament strikes on the left side of the wound, ion fluxes and fluences are larger by factors of 100–1000 on the right side of the wound (and vice versa). This is due to the inability of the spreading plasma to conformally adhere to the topography of the cells, as the Debye length, approximately 1–2 μm is too large. As the filament spreads on the surface towards the wound, the direction of the electric field at the head of the filament is parallel to the surface. As the filament enters the wound, the electric field retains a

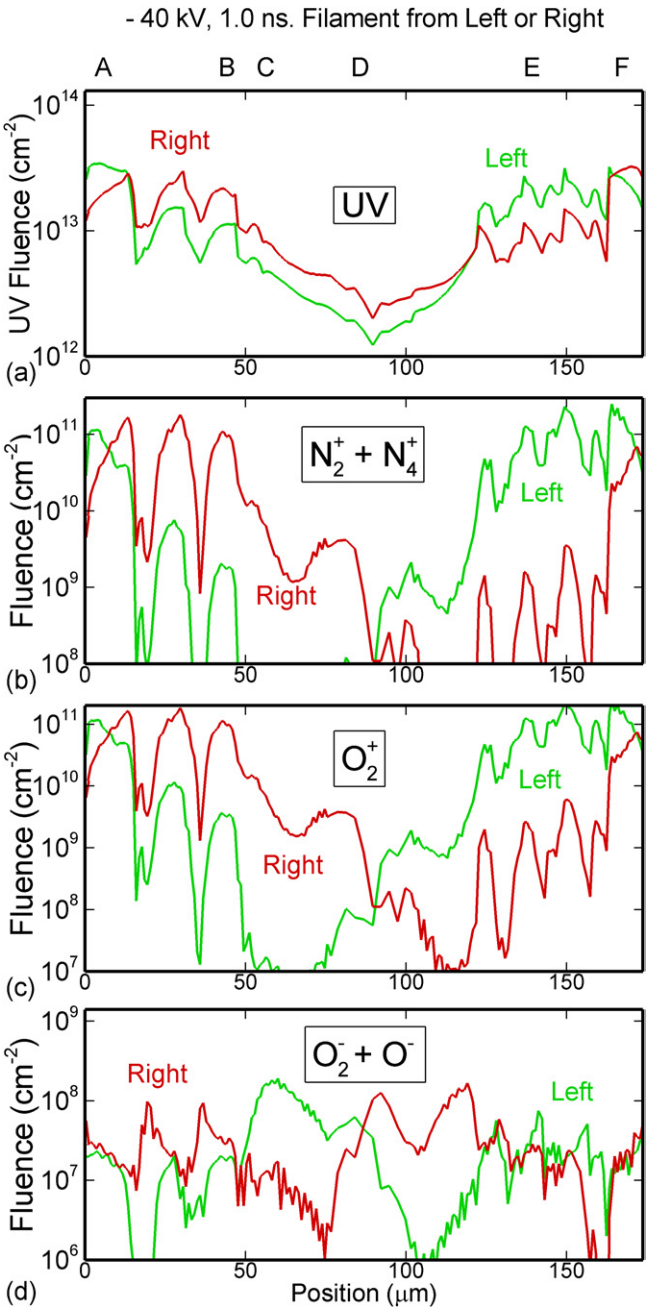

Figure 17. UV and ion fluences recorded at 1.0 ns for plasma filaments striking to the left (green curve) and to the right (red curve) of the wound. (*a*) UV photon flux (*b*) sum of N_2^+ and N_4^+ (*c*) O_2^+, and (*e*) sum of O^- and O_2^- fluxes. Fluences are recorded along the A to F surface (see figure 1(*c*)). Conditions are humid air ($N_2/O_2/H_2O$ = 79/20/1) and −40 kV.

large component directed towards the uncharged surfaces on the opposite side of the wound. The end result is the launching of the filament across the wound.

The flux and fluence of photons into the wound are less sensitive to the location of the filaments than for ions. Although there is an asymmetry, the differences from side-to-side are only factors of 2–4 as opposed to factors of hundreds. This lack of sensitivity results from the fact that photons striking a given surface site originate from 10s to 100s μm from that surface site and so reflect the integrated excitation over a larger volume than do fluxes for ions. The ions that strike a surface on these time scales originate from only a few micrometres from the surface, and so reflect much more local conditions.

On the plasma time scale, fluences of ROS and RNS do have asymmetries, as shown in figure 18, of up to a factor of 10–100 from side-to-side, and more so in shadowed regions of the wound. On the plasma time scale, the ROS fluences are dominated by atomic O, $O_2(^1\Delta)$ and OH (the fluence of ozone is negligible), and RNS is dominated by N_2^*, as NO is not directly produced by the plasma. For neutral radicals, post-pulse diffusion makes the location of the filament less important, as shown by the ROS and RNS densities in figure 19 and the fluences at 0.5 ms in figure 20. Although there are side-to-side differences in densities and fluences depending on which side of the wound the filament strikes, these differences are less than a factor of two. (Note the small dynamic range in the plots.) The differences result from the majority of the radicals being created by electron impact or subsequent reactions being on one side of the wound and then diffusing *over* the wound to volumes having lower densities. In this sense the fluxes and fluences to the surface reflect the gradient of the radical fluxes which drive the diffusion. In any event, the differences for fluxes across the wound are small with the exception of O atoms fluxes which react to form ozone prior to diffusing deeply into the wound. As in the symmetric cases, O_3 and $O_2(^1\Delta)$ have the largest fluences to the wound—the former because it is formed during the interpulse period and the latter because of its long lifetime.

5. Global modelling and long-term fluxes

The results just discussed provide insights into the details of plasma interaction with tissue and small wounds. In actual DBD treatment of tissue, devices are operated at up to many kHz and expose the tissue over many seconds. Due to the computational burden, it is not practical to investigate long-term exposure of tissue to air plasmas including a complete reaction mechanism over thousands of pulses using multidimensional modelling down to the cellular level. Global modelling is ideal for investigating these trends and for contrasting the results with those implied by the more detailed single-pulse 2D modelling. Global modelling was performed for an atmospheric-pressure air plasma sustained in $N_2/O_2/H_2O$ = 79/20/1.0. The repetition rate is 10 kHz and 500 pulses were computed. The gap between dielectrics is 2 mm and the series capacitance is 1 pF cm^{-2}. The average energy deposition/pulse is about 1 mJ cm^{-3}. These parameters were chosen to deliver approximately the same energy/pulse as in the 2D model. The choice of frequency in the global model was made for convenience in order to provide self-consistent long-term densities to contrast with the 2d model.

Ions during the 500th DBD discharge pulse are shown in figure 21 while a selection of neutral species are shown in figure 22. The current pulse lasts for about 2 ns. It is during this time that the primary ions (N_2^+, O_2^+, H_2O^+) are produced by direct electron impact on the feedstock gases. The dominant primary positive ion is O_2^+ reaching a volume averaged peak density of (1–2) × 10^{12} cm^{-3}, contributing

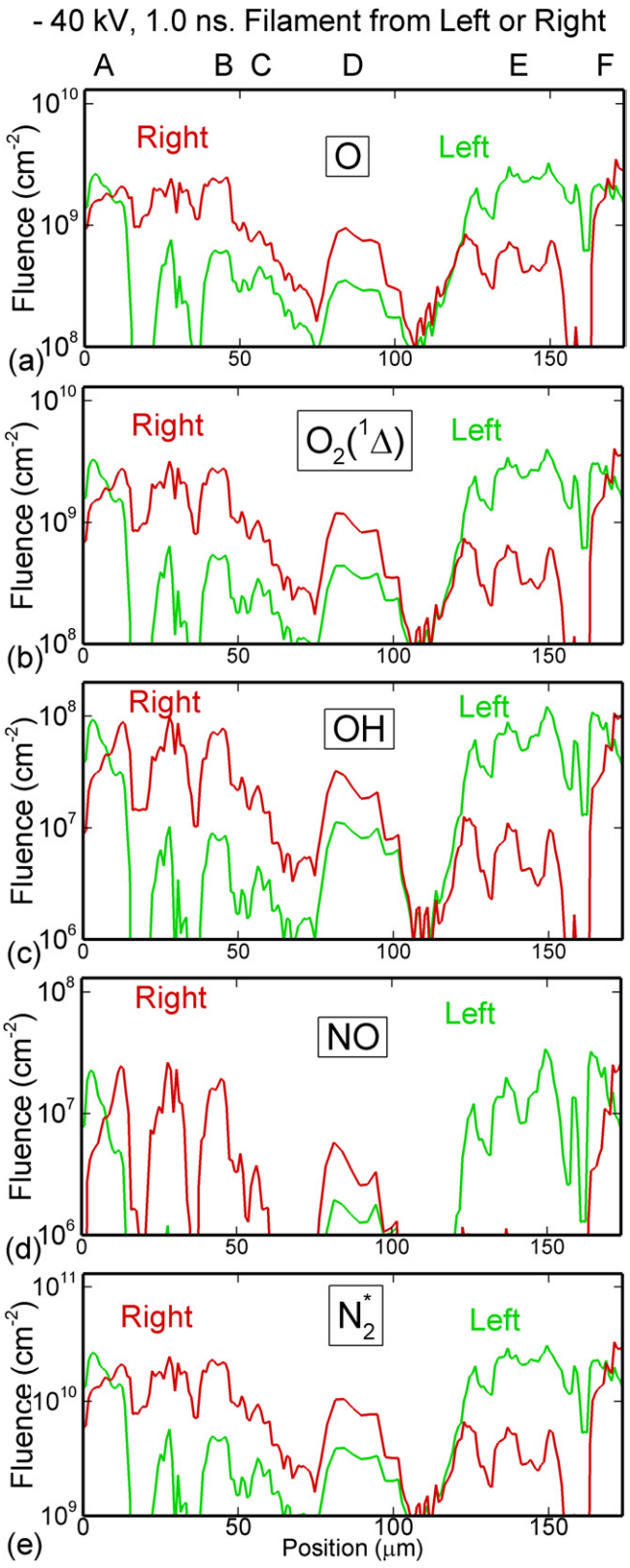

Figure 18. ROS and RNS fluences recorded at 1.0 ns for plasma filaments striking to the left (green curve) and to the right (red curve) of the wound. (*a*) O, (*b*) $O_2(^1\Delta)$, (*c*) OH, (*d*) NO and (*e*) N_2^*. Fluences are recorded along the A to F surface (see figure 1(*c*)). Conditions are humid air ($N_2/O_2/H_2O = 79/20/1$) and −40 kV.

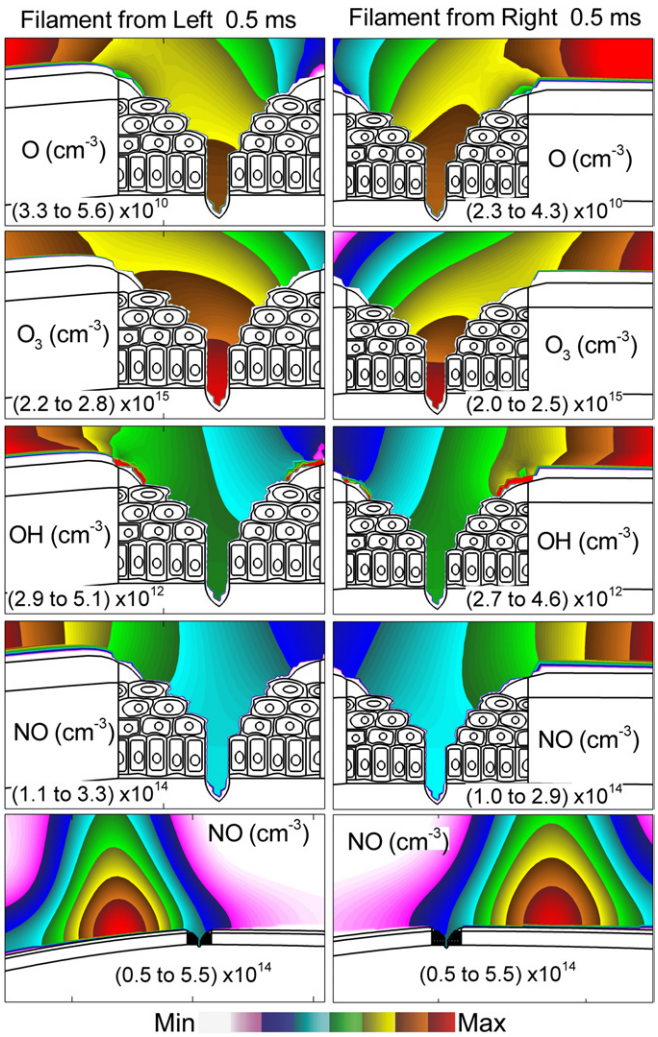

Figure 19. Densities of ROS and NRS inside the wound recorded at 0.5 ms for the plasma filament located (left column) to the left and (right column) to the right of the wound. From top to bottom—O, O_3, OH, and NO. Note the narrow dynamic range of the plots. The bottom row shows a larger scale view of the NO density. On the scale of the wound, these densities are essentially uniform. Conditions are humid air ($N_2/O_2/H_2O = 79/20/1$) and −40 kV. The range of values plotted is indicated in each frame.

to a peak average plasma density of 4×10^{12} cm^{-3}. These values are comparable to those predicted in other global models of air plasma chemistry for similar conditions [38] but the densities are significantly lower than those predicted within the streamer by the 2D model. This discrepancy results from the global models having significantly smaller volumetric power deposition (W cm^{-3}) compared to the streamer. The global models also lack the improved ionization efficiency that is produced in the avalanche front of the streamer, a phenomenon that is difficult to include in a global model. However, on a specific ionization efficiency basis (that is, eV/ion or eV/radical) the ion inventory predicted by the 2D and global modelling are comparable.

After termination of the current pulse, production of the primary ions by electron impact also terminates, and the primary ions are quickly depleted by charge exchange reactions within a few ns. In the presence of water vapour the end product

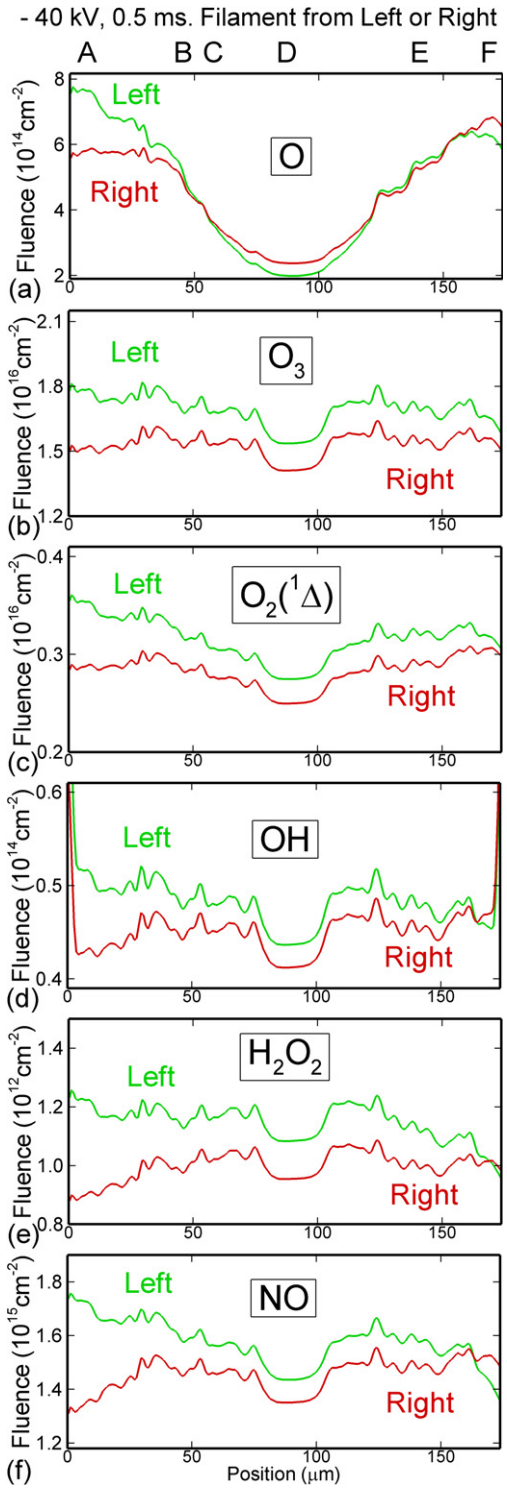

Figure 20. ROS and RNS fluences recorded at 0.5 ms for plasma filaments striking to the left (green curve) and to the right (red curve) of the wound. (*a*) O, (*b*) O_3, (*c*) $O_2(^1\Delta)$, (*d*) OH, (*e*) H_2O_2, and (*f*) NO. Fluences are recorded along the A to F surface (see figure 1(*c*)). Conditions are humid air ($N_2/O_2/H_2O = 79/20/1$) and −40 kV.

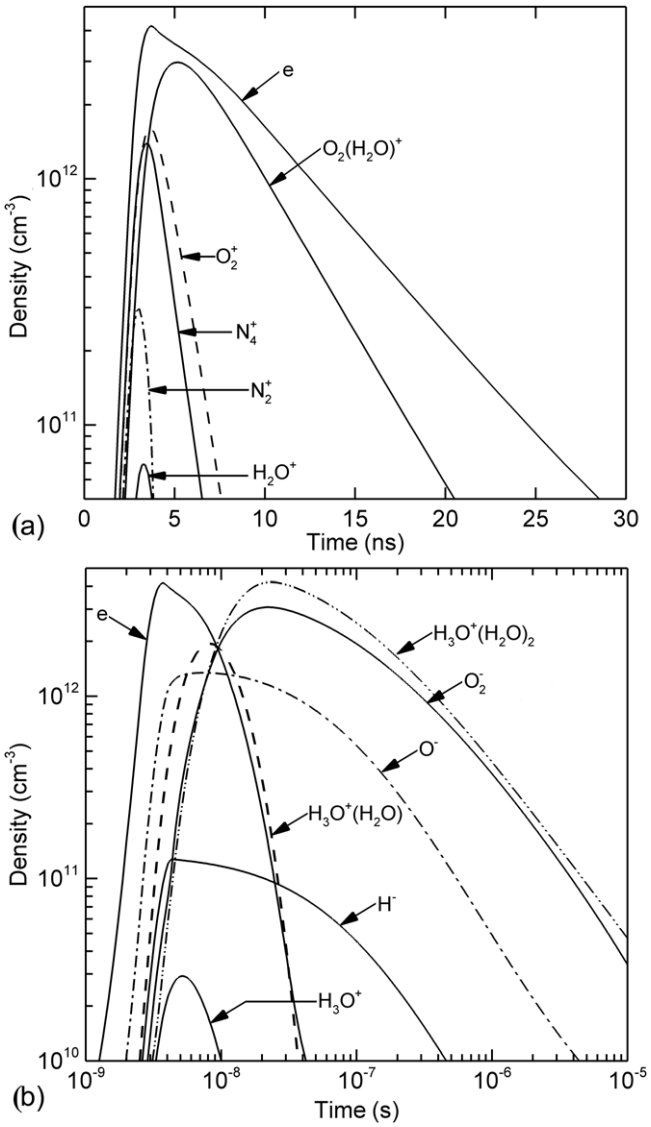

Figure 21. Densities of electrons and ions during the first (*a*) 30 ns and (*b*) 10 μs of the 500th successive discharge pulse in humid air. These results were obtained with the global kinetics model. Conversion from primary ions to water-cluster ions occurs in about 5–10 ns.

of these charge exchange reactions are water-cluster ions, which in our reaction mechanism produces a terminal positive ion of $H_3O^+(H_2O)_2$. Electrons are depleted by electron-ion recombination and attachment, resulting in the vast majority of negative charge residing in O_2^- and O^-. Ion–ion neutralization (and to a lesser extent diffusion losses) requires more than 10 μs. The shorter time scale, multidimensional calculations capture the dynamics of the primary ions and first charge exchange products. The calculations do not capture the long-term exposure of the tissue to the terminal water-cluster ions and O_2^-, the latter of which is recognized as being biologically important.

The differences in specific power deposition (W cm^{-3}) between the global and streamer models for electron impact processes produce large differences in peak ion densities but should not be terribly important for short pulses. In the absence of multistep ionization processes, the majority of the plasma chemistry during the pulse scales linearly with the electron density. So for short pulses where ground state ionization dominates, the nonlinear aspects of multistep ionization processes from excited states produced during that pulse are not critical. As long as the energy deposition is the same in the global and 2D models, then the total

inventory of ions produced should also be the same, though this inventory is probably enhanced in the streamer model by the improved efficiency of the ionization wave. Since diffusion and quenching reactions during the interpulse afterglow period diminish excited state densities, the next current pulse is also dominated by ionization from ground states (or slightly enhanced by ionization of vibrationally excited or metastable states that accumulate pulse-to-pulse). The exceptions to these trends include the rate of electron-recombination and ion–ion neutralization, which scale with the square of plasma density. Since the plasma density is higher in the streamer the initial rate of decay of plasma species will be greater than predicted by the global model.

The behaviour of the neutral radicals and excited species can be divided into three categories. The first includes species which are pulse periodic. That is, the species are produced during the discharge pulse and decay away to small values before the next discharge pulse. Such species include $N_2(A)$ which is dominantly quenched by dissociative excitation transfer to O_2 to produce O atoms. These species, shown in figure 22(*a*), are also well represented by the 2D single-pulse simulations. A second category of neutral radicals and products are quasi-pulse-periodic species. These are species that obtain a steady state background density but whose densities are modulated during the pulse cycle. These species, which include O, $N_2(v)$, OH and HO_2 (shown in figures 22(*a*) and (*b*)), may be well represented by the 2D-single-pulse (and afterglow) model if their modulation is large. For example, O atoms are modulated by a factor of 10 during the discharge (and would be well represented) and while OH is modulated by only a factor of 2 (and would not be well represented).

The final category is for species that accumulate over long times. These species include O_3, H_2O_2, $O_2(^1\Delta)$, HNO_2, HNO_3, NO and NO_2, as shown in figures 22(*b*) and (*c*). Since the densities of these species accumulate over time and so have significant densities at the beginning of the discharge pulse, they are poorly represented by the 2D single-pulse and afterglow. Having said that, the reason why these species accumulate on a pulse-to-pulse basis (or evolve to have a high density in the steady state) is that they tend to be only mildly reacting with other gas phase species. On the spatial scale of the streamer, after tens of pulses, these species have nearly uniform back ground densities by virtue of diffusion.

A compromise modelling strategy is to use global modelling to obtain the densities of quasi-pulse periodic and cumulative species after many pulses, and use those densities as initial conditions for the 2D single-pulse and afterglow calculation. This strategy was followed by using as initial conditions for the 2D model the radical and product densities at the end of the afterglow for the 500th pulse from the global kinetics model. These initial densities, listed in table 3, were uniformly distributed in the volume of the 2D model through which the streamer would propagate. A comparison of the fluences onto the wound for the 1st and 500th pulse after 0.5 ms is in figure 23.

The mole fractions of the ions incident onto the wound for the 1st and 500th pulse did not significantly change however the magnitude of the fluxes uniformly increased by a few

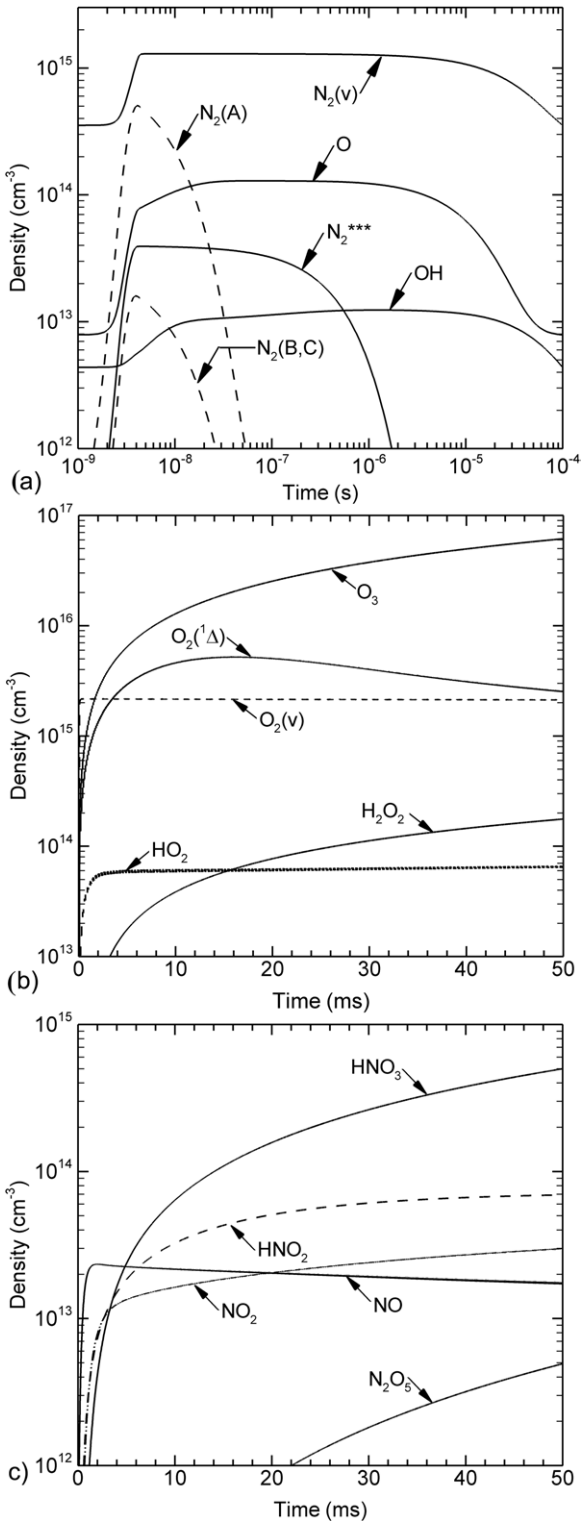

Figure 22. Densities of excited states, radicals and products over the first 500 pulses for a DBD operating in humid air at 10 kHz. (*a*) Densities of pulse periodic and quasi-pulse periodic excited states and radicals for the 500th pulse and afterglow. Densities of radicals and products that reach a steady state from the first to 500th pulse for (*b*) ROS and (*c*) RNS.

to 5%. Although small, this increase is largely due to the small initial mole fraction of more easily ionized species, in this case principally $O_2(^1\Delta)$. The fluences of accumulating species, such as H_2O_2 and O_3, increased in proportion to the

Table 3. Initial densities for the 2D calculation of the 500th pulse.

Species	Density (cm^{-3})	Species	Density (cm^{-3})
N	5.7×10^{13}	OH	4.3×10^{12}
$O_2(^1\Delta)$	2.5×10^{15}	HO_2	6.4×10^{13}
O	7.9×10^{12}	H_2O_2	1.7×10^{14}
O_3	6.1×10^{16}	NO	1.7×10^{13}
H_2	6.2×10^{13}	NO_2	3.0×10^{13}

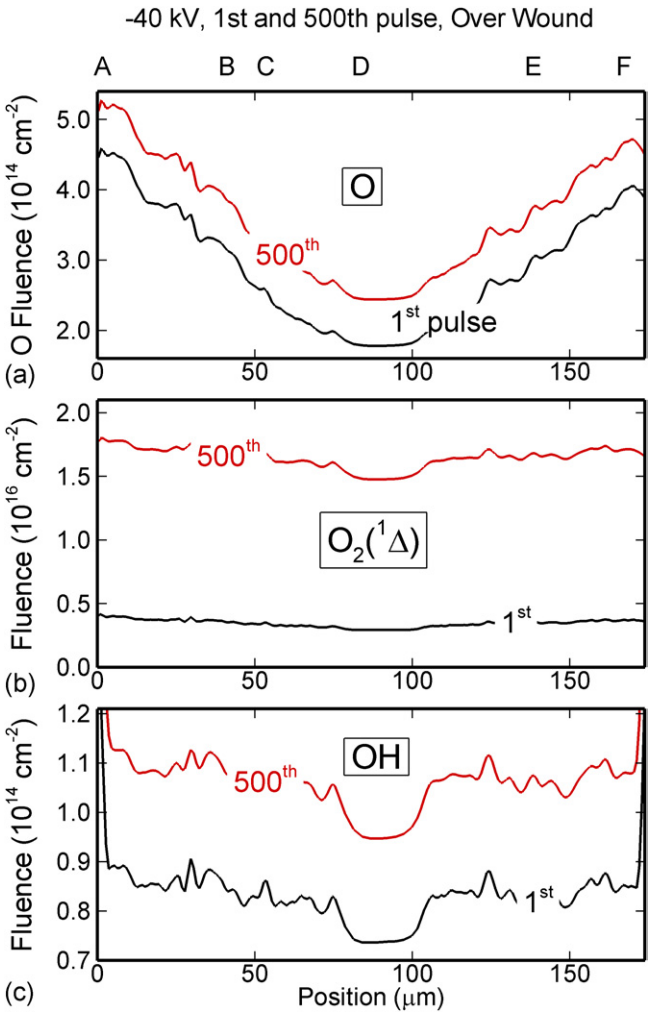

Figure 23. ROS fluences into the wound recorded for 0.5 ms after the 1st and 500th pulse computed with the two-dimensional model. (*a*) O, (*b*) $O_2(^1\Delta)$ and (*c*) OH. Fluences are recorded along the A to F surface (see figure 1(*c*)). The initial conditions for the 1st pulse are humid air without radical or excited state species. The initial conditions for the 500th pulse were humid air with a uniform distribution of radicals and products obtained from the global kinetics model.

increase in their density over the 500 pulses. For example, the fluence for H_2O_2 increased from 4×10^{12} cm^{-2} during the afterglow following the first pulse to 1.2×10^{15} cm^{-2} during the afterglow following the 500th pulse. However, the fluence of a subset of the ROS species, O, $O_2(^1\Delta)$ and OH, changed little between the 1st and 500th pulse as shown in figure 23. O and OH are pulse-periodic species whose densities increase and decrease over each pulse and afterglow. The fluence per pulse of these species is nearly constant on a pulse-to-pulse basis. In spite of the initially uniform background of $O_2(^1\Delta)$, its fluence increases only by a factor of 4. This is due to the $O_2(^1\Delta)$ being produced in close proximity of the wound and by the spreading of the plasma along the surface. In the global model, radical densities are volume averaged quantities. This local production of $O_2(^1\Delta)$ near the surface disproportionately increases fluxes (and fluence) for a given rate of volume averaged production.

6. Concluding remarks

The interactions of plasma filaments, as produced in a DBD, with human tissue having a small dry wound have been computationally investigated using two-dimensional streamer and global models. We found that the location of the streamer relative to the wound is important to the fluxes (and fluence) of ions and photons due to the intrinsically more directional and shorter lifetimes of these species. The effects of shadowing, charging and spreading of the plasma on the surface of the skin into the wound can result in non-uniform treatment of the cells. This is also true for radicals directly produced by electron impact on the time scale of the filament. However, interpulse diffusion mediates these non-uniformities and the majority of neutral radicals produce uniform fluences onto the wound. For operating conditions typical of DBDs as used in plasma medicine, the fluxes of RNS and ROS species produce fluences over a few seconds of treatment that are nearly equal to the surface site density. These results imply that the biological reactivity of these systems is limited by the reaction probabilities and not by the availability of radical fluxes.

In many instances of wound treatment, the wound is wet—covered in whole or part by a liquid resembling blood serum. Due to the change in dielectric properties and topography of the wound produced by the liquid, there can be subtle changes in the shape of the streamer as it approaches the wound and so changes in the production of radicals. The delivery of ROS and RNS to the surface of the cell is mediated by the intervening liquid layer and the interaction of dissolved ROS with hydrocarbon proteins (termed RH) in the liquid. For example, the majority of O and OH penetrating into the liquid will quickly react with the RH in the liquid by abstracting H atoms to form alkyl sites, R•, which then subsequently react with other species. The discussion of such processes will be addressed in upcoming publications.

In comparison to multi-pulse global modelling, we found that single-pulse streamer models likely capture the dynamics of many of the shorter lived radicals, excited species and ions, but do not capture the long-term (many tens to hundreds of seconds) evolution of RNS and ROS. The fluences of pulse-periodic species (such as O and OH) are nearly constant from pulse to pulse whereas the per pulse fluences of accumulating species such as H_2O_2 and O_3, increase in proportion to the increase in their density over many hundreds to thousands of pulses. When the 2D streamer model is executed using densities from the global model as initial conditions, we found moderate increases in the fluences of ions and short lived radicals. These increases are a result of the accumulation of more easily ionized species and electronically excited

metastable states, such as $O_2(^1\Delta)$. When operating the DBD at constant voltage, the resulting small decrease in critical electric field resulting from the accumulation of excited states produces a proportional increase in the over-voltage, and so a more intense streamer.

We hesitate to extrapolate these results to wounds of dramatically different sizes and different topography, however some generalizations can be made. The delivery of ion and photon fluxes to the surface of the wound are more sensitive to the relative location of the streamer to the wound, the size of the wound and the topography of the wound than neutral fluxes. Even when averaged over many hundreds or thousands of pulses, self-organization of the filaments may produce spatially dependent fluences that depend on size and topography of the wound. The fluences of neutral radicals are much less sensitive to these effects provided that the treatment times are long compared to the time required for radicals to diffuse the distance between streamers (either in the volume of the gas or along the surface).

Acknowledgment

This work was supported by the US Department of Energy Office of Fusion Energy Science and the National Science Foundation.

References

[1] Kong M G, Kroesen G, Morfill G, Nosenko T, Shimizu T, van Dijk J and Zimmermann J L 2009 Plasma medicine: an introductory review *New J. Phys.* **11** 115012
[2] Morfill G E, Kong M G and Zimmermann J L 2009 Focus on plasma medicine *New J. Phys.* **11** 115011
[3] Fridman G, Shekhter A B, Vasilets V N, Friedman G, Gutsol A and Fridman A 2008 Applied plasma medicine *Plasma Process. Polym.* **5** 503
[4] Laroussi M, Mendis D A and Rosenberg M 2003 Plasma interaction with microbes *New J. Phys.* **5** 41
[5] Boudam M K, Moisan M, Saoudi B, Popovici C, Gherardi N and Massines F 2006 Bacterial spore inactivation by atmospheric-pressure plasmas in the presence or absence of UV photons as obtained with the same gas mixture *J. Phys. D: Appl Phys.* **39** 3494
[6] Laroussi M 2009 Low-temperature plasmas for medicine *IEEE Trans. Plasma Sci.* **37** 714
[7] Deilmann M, Halfmann H, Bibinov N, Wunderlich J and Awakowicz P 2008 Low-pressure microwave plasma sterilization of polyethylene terephthalate bottles *J. Food Prot.* **71** 2119
[8] Stoffels E, Sakiyama Y and Graves D 2008 Cold atmospheric plasma: Charged species and their interactions with cells and tissues *IEEE Trans. Plasma Sci.* **36** 1441
[9] Kieft I E, Kurdi M and Stoffels E 2006 Reattachment and apoptosis after plasma-needle treatment of cultured cells *IEEE Trans. Plasma Sci.* **34** 1331
[10] Kieft I E, Darios D, Roks A J M and Stoffels-Adamowicz E 2005 Plasma treatment of mammalian vascular cells: A quantitative description *IEEE Trans. Plasma Sci.* **33** 771
[11] Fridman G, Peddinghaus M, Ayan H, Fridman A, Balasubramanian M, Gutsol A, Brooks A and Friedman G 2006 Blood coagulation and living tissue sterilization by floating electrode dielectric barrier discharge in air *Plasma Chem. Plasma Process.* **26** 425
[12] Fridman G, Shereshevsky A, Jost M M, Brooks A D, Fridman A, Gutsol A, Vasilets V and Friedman G 2007 Floating electrode dielectric barrier discharge plasma in air promoting apoptotic behavior in melanoma skin cancer cell lines *Plasma Chem. Plasma Process.* **27** 163
[13] Lee S M, Hong Y J, Seo Y S, Iza F, Kim G Ch and Lee J K 2009 Simulations of biomedical atmospheric-pressure discharges *Comput. Phys. Commun.* **180** 636
[14] Kim G C, Kim G J, Park S R, Jeon S M, Seo H J, Iza F and Lee J K 2009 Air plasma coupled with antibody-conjugated nanoparticles: a new weapon against cancer *J. Phys. D: Appl. Phys.* **42** 032005
[15] Deng X, Shi J J and Kong M G 2007 Protein destruction by a helium atmospheric pressure glow discharge: capability and mechanisms *J. Appl. Phys.* **101** 074701
[16] Laroussi M 2002 Non-thermal decontamination of biological media by atmospheric pressure plasmas: review, analysis and prospects *IEEE Trans. Plasma Sci.* **30** 1409
[17] Sladek R E J and Stoffels E 2005 Deactivation of *Escherichia coli* by the plasma needle *J. Phys. D: Appl. Phys.* **38** 1716–21
[18] Schoenbach K H, Beebe S J and Buescher E S 2001 Intracellular effect of ultrashort electrical pulses *J. Bioelectromagn.* **22** 440
[19] Beebe S J, Fox P M, Rec L J, Somers K, Stark R H and Schoenbach K H 2002 Nanosecond pulsed electric field (nsPEF) effects on cells and tissues: apoptosis induction and tumor growth inhibition *IEEE Trans. Plasma Sci.* **30** 286
[20] Shekhter A B, Serezhenkov V A, Rudenko T G, Pekshev A V and Vanin A F 2005 Beneficial effect of gaseous nitric oxide on the healing of skin wounds *Nitric oxide* **12** 210–9
[21] Sweet F, Kao M S, Lee S C, Hagar W L and Sweet W E 1980 Ozone selectively inhibits growth of human cancer cells *Science* **209** 931
[22] Sato T, Ochiai S and Urayama T 2009 Generation and transport mechanism of chemical species by a post-discharge flow for inactivation of bacteria *New J. Phys.* **11** 115018
[23] Nosenko T, Shimizu T and Morfill G E 2009 Designing plasmas for chronic wound disinfection *New J. Phys.* **11** 115013
[24] Goree J, Liu B, Drake D and Stoffels E 2006 Killing of *S. mutans* bacteria using a plasma needle at atmospheric pressure *IEEE Trans. Plasma Sci.* **34** 1317
[25] Park G, Lee H, Kim G and Lee J K 2008 Global model of He/O_2 and Ar/O_2 atmospheric pressure glow discharges *Plasma Process. Polym.* **5** 569–76
[26] Liu D X, Rong M Z, Wang X H, Iza F, Kong M G and Bruggeman P 2010 Main species and physicochemical processes in cold atmospheric-pressure He/O_2 plasmas *Plasma Process. Polym.* **7** 846–65
[27] Liu D X, P Bruggeman, Iza F, Rong M Z and Kong M G 2010 Global model of low-temperature atmospheric-pressure He + H_2O plasmas *Plasma Sources Sci. Technol.* **19** 025018
[28] Gentile A C and Kushner M J 1995 Reaction chemistry and optimization of plasma remediation of N_xO_y from gas Streams *J. Appl. Phys.* **78** 2074
[29] Filimonova E A, Amirov R H, Kim H T and Park I H 2000 Comparative modeling of NO*x* and SO_2 removal from pollutant gases using pulsed-corona and silent discharges *J. Phys. D: Appl. Phys.* **33** 1716
[30] Klett C, Touchard S, Vega-Gonzalez A, Redolfi M, Bonnin X, Hassouni K and Duten X 2012 Experimental and modeling study of the oxidation of acetaldehyde in an atmospheric-pressure pulsed corona discharge *Plasma Sources Sci. Technol.* **21** 045001
[31] Starikovskaia S M 2006 Plasma assisted ignition and combustion *J. Phys. D: Appl. Phys.* **39** R265
[32] Aleksandrov N L, Kindysheva S V, Kosarev I N, Starikovskaia S M and Starikovskii A Yu 2009 Mechanism

of ignition by non-equilibrium plasma *Proc. Combust. Inst.* **32** 205–12
[33] Yin Z, Takashima K and Igor V Adamovich 2011 Ignition time measurements in repetitive nanosecond pulse hydrogen–air plasmas at elevated initial temperatures *IEEE Trans. Plasma Sci.* **39** 3269
[34] Starikovskii A Y, Anikin N B, Kosarev I N, Mintoussov E I, Nudnova M M, Rakitin A E, Roupassov D V, Starikovskaia S M and Zhukov V P 2008 Nanosecond-pulsed discharges for plasma-assisted combustion and aerodynamics *J. Propulsion Power* **24** 1182
[35] Kossyi I A, Kostinsky A Y, Matveyev A A and Silakov V P 1992 Kinetic scheme of the non-equilibrium discharge in nitrogen–oxygen mixtures *Plasma Sources Sci. Technol.* **1** 207
[36] Sieck L W, Buckley T J, Herron J T and Green D S 2001 Pulsed electron-beam ionization of humid air and humid air/toluene mixtures: time-resolved cationic kinetics and comparisons with predictive models *Plasma Chem. Plasma Process.* **21** 441
[37] Herron J T and Green D S 2001 Chemical kinetics database and predictive schemes for nonthermal humid air plasma chemistry: II. Neutral species reactions *Plasma Chem. Plasma Process.* **21** 459
[38] Sakiyama Y, Graves D B, Chang H-W, Shimizu T and Gregor E Morfill 2012 Plasma chemistry model of surface micro-discharge in humid air and dynamics of reactive neutral species *J. Phys. D: Appl. Phys.* **45** 425201
[39] Shimizu T, Sakiyama Y, Graves D B, Zimmermann J L and Morfill G E 2012 Dynamics of ozone generation and mode transition in air surface micro-discharge plasma at atmospheric pressure *New J. Phys.* **14** 103028
[40] Murakami T, Niemi K, Gans T, Connell D O and Graham W G 2013 Chemical kinetics and reactive species in atmospheric pressure helium-oxygen plasmas with humid air impurities *Plasma Sources Sci. Techniol.* **22** in press
[41] Murakami T, Niemi K, Gans T, Connell D O and Graham W G 2012 Plasma chemistry in atmospheric-pressure He–O_2 plasmas in humid air *Proc. 21st Europhysics Conf. on the Atomic and Molecular Physics of Ionized Gases (Viana do Castelo, Portugal, 10–14 July)*
[42] Xiong Z and Kushner M J 2010 Surface corona-bar discharges for production of pre-ionizing UV light for pulsed high pressure plasmas *J. Phys. D: Appl. Phys.* **43** 505204
[43] Naidis G V 2006 On photoionization produced by discharges in air *Plasma Sources Sci Technol.* **15** 253
[44] Bourdon A, Pasko V P, Liu N Y, Célestin S, P Ségur and Marode E 2007 Efficient models for photoionization produced by non-thermal gas discharges in air based on radiative transfer and the Helmholtz equations *Plasma Sources Sci. Technol.* **16** 656
[45] Liu N, Celestin S, Bourdon A, Pasko V P, Ségur P and Marode E 2007 Application of photoionization models based on radiative transfer and the Helmholtz equations to studies of streamers in weak electric fields *Appl. Phys. Lett.* **91** 211501
[46] Luque A, Ebert U, Montijn C and Hundsdorfer W 2007 Photoionisation in negative streamers: fast computations and two propagation modes *Appl. Phys. Lett.* **90** 081501
[47] Nudnova M M and Starikovskii A Yu 2008 Streamer head structure: role of ionization and photoionization *J. Phys. D: Appl. Phys.* **41** 234003
[48] Dorai R 2002 Modeling of atmospheric pressure plasma processing of gases and surfaces *PhD Thesis* University of Illinois (http://uigelz.eecs.umich.edu/ theses.html)
[49] Babaeva N Yu and Kushner M J 2010 Intracellular electric fields produced by dielectric barrier discharge treatment of skin *J. Phys. D: Appl. Phys.* **43** 185206
[50] Traylor M J, Pavlovich M J, Karim S, Hait P, Sakiyama Y, Clark D S and Graves D B 2011 Long-term antibacterial efficacy of air plasma-activated water *J. Phys. D: Appl. Phys* **44** 472001
[51] Stafford S D and Mark Kushner 2004 $O_2(^1\Delta)$ Production in He/O_2 mixtures in flowing low pressure plasmas *J. Appl. Phys.* **96** 2451
[52] Feldman Y, Ermolina I and Hayashi Y 2003 Time domain dielectric spectroscopy study of biological systems *IEEE Trans. Dielectr. Electr. Insul.* **10** 728
[53] Ermolina I, Polevaya Y, Feldman Y, Ginzburg B and Schlesinger M 2001 Study of normal and malignant white blood cells by time domain dielectric spectroscopy *IEEE Trans. Dielectr. Electr. Insul.* **8** 253
[54] Papageorghiou L, Panousis E, Loiseau J F, Spyrou N and Held B 2009 Two-dimensional modeling of a nitrogen dielectric barrier discharge (DBD) at atmospheric pressure: filament dynamics with the dielectric barrier on the cathode *J. Phys. D: Appl. Phys.* **42** 105201
[55] Kelemen M V and Sharpe J E E 1979 Controlled cell disruption: a comparison of the forces required to disrupt different micro-organisms *J. Cell Sci.* **35** 431
[56] Ingber D E and Folkman J 1989 Mechanochemical switching between growth and differentiation during fibroblast growth factor-stimulated angiogenesis in vitro: role of extracellular matrix *J. Cell Biol.* **109** 317
[57] Stollenwerk L 2009 Interaction of current filaments in dielectric barrier discharges with relation to surface charge distributions *New J. Phys.* **11** 103034
[58] Celestin S, Canes-Boussard G, Guaitella O, Bourdon A and Rousseau A 2008 Influence of the charges deposition on the spatio-temporal self-organization of streamers in a DBD *J. Phys. D: Appl. Phys.* **41** 205214